Computers and Fluids 247 (2022) 105634

Contents lists available at ScienceDirect

Computers and Fluids

journal homepage: www.elsevier.com/locate/compfluid

Artificial compressibility approaches in flux reconstruction for incompressible viscous flow simulations

W. Trojak [a,*], N.R. Vadlamani [b], J. Tyacke [c], F.D. Witherden [d], A. Jameson [e]

[a] Department of Aeronautics, Imperial College London, London, SW7 2AZ, United Kingdom
[b] Department of Aerospace Engineering, IIT Madras, Chennai, 600036, India
[c] Department of Mechanical and Aerospace Engineering, Brunel University, Uxbridge, UB8 3PH, United Kingdom
[d] Department of Ocean Engineering, Texas A&M University, College Station, TX 77843, United States of America
[e] Department of Aerospace Engineering, Texas A&M University, College Station, TX 77843, United States of America

ARTICLE INFO

Keywords:
Artificial compressibility
Flux reconstruction
High order
Incompressible flow

ABSTRACT

Artificial compressibility methods intend to offer divergence-free free velocity fields at the incompressible limit for compressible solvers. Three major approaches for this are compared within a high-order flux reconstruction framework: the established method (ACM) of Chorin (1967) and a new entropically damped method (EDAC) of Clausen (2013) which can keep velocity divergence sufficiently low to be run explicitly without the non-linear solver required by ACM. Furthermore, the ACM approach with hyperbolised diffusion is investigated. The accuracy and computational efficiency of these methods is investigated for a series of turbulent test cases over a range of Reynolds numbers. It is found for EDAC that velocity divergence scales linearly with the square root of compressibility, whereas for ACM a clear relation is not observed. EDAC is found to accurately resolve the low Reynolds number Taylor–Green vortex case; however, for the circular cylinder at Reynolds number 3900, earlier transition of the free shear-layer is observed due to an over-production of the turbulence kinetic energy. This over production of turbulent kinetic energy is attributed to the increased spatial pressure gradients of the EDAC method, and similar behaviour is observed for an aerofoil at Reynolds number 60 000 with an attached transitional boundary layer. These issues were not observed for the other ACM approaches. It is concluded that hyperbolic diffusion of ACM can be beneficial in terms of convergence but at the cost of case setup time, and EDAC can be a time efficient method for unsteady incompressible flows. However, care must be taken when reducing the stiffness of EDAC as the resulting pressure fluctuations can have a significant impact on transition.

1. Introduction

There is a growing desire across many industries to gain detailed insight into transient flow phenomena. In many cases, however, this is difficult to achieve with experimentation due to high costs and difficulties observing key physics. Recently, there has been growing interest in high-order methods in engineering applications as, compared to low order approaches, the resolution and computational efficiencies achievable can make many intractable problems tractable [1]. A further factor in this success has a shifting desire from modelled simulations, of which Reynolds averaged Navier–Stokes (RANS) may be considered representative, to the scale-resolving methods such as large eddy simulation (LES). Although RANS has seen great success in several industrially relevant problems, such as transonic wing shape optimisation [2] and stall prediction in transonic fans [3]. The approximations of the model limit its accuracy for various problems involving transition, strong streamline curvature, and relaminarization. Durbin [4] discusses recent advances, remaining and new challenges to RANS turbulence modelling as application areas widen. Scale resolving simulations, on the other hand, attempt to directly resolve the majority of the physical length scales on the grid. Such approaches can elucidate complex flow physics, especially those rooted in the small scale motions. In explicit LES methods, the effect of unresolved length scales are modelled using a sub-grid scale (SGS) model, often coupled to a filter. An alternative paradigm that has gained wider adoption, is implicit LES (ILES) where no SGS model is used and dissipation of the small scales is handled implicitly by the numerical dissipation of the discretisation. The spatial scheme we will use to perform ILES is the high-order flux reconstruction method of Huynh [5], as implemented in PyFR [6].

A challenge occurs in the limit as Mach number, M, tends to zero. The compressible flow equations become increasingly stiff, ultimately

* Corresponding author.
E-mail addresses: wtrojak@ic.ac.uk (W. Trojak), nrv@smail.iitm.ac.in (N.R. Vadlamani), James.Tyacke@brunel.ac.uk (J. Tyacke).

https://doi.org/10.1016/j.compfluid.2022.105634
Received 15 November 2021; Received in revised form 18 July 2022; Accepted 9 August 2022
Available online 27 August 2022

resulting in an elliptic equation for the pressure field at $M = 0$. If the compressible Navier–Stokes equations are used in this low Mach limit, the stiffness can lead to prohibitively expensive calculations. In the case of the method of Roe [7] it also leads to excessive numerical dissipation. These problems can be alleviated by the use of a low Mach preconditioners, such as that of Turkel [8]. Alternatively, in the incompressible regime a separate solver is used to solve the pressure Poisson equation. However, it is non-trivial to produce a scalable solver for the Poisson equation, although new methods such as that of Fortunato and Townsend [9] are beginning to confront aspects of this. Furthermore, within finite element methods ensuring solution compatibility requires detailed analysis that is dependent on order and element type, among other factors [10].

A single solver is preferable to make use of established tools and optimisations, and to simplify work flows. Artificial compressibility approaches allows the use of established compressible tool to calculated state solutions of incompressible flows. The first such method was the artificial compressibility method (ACM) of Chorin [11], which can be interpreted as assuming constant entropy together with an artificial compressibility to relax the pressure and velocity field onto a divergence free solution. ACM was extended to the calculation of unsteady flows by Rogers et al. [12] by using it as a method to solve the implicit equations for each physical time step. Later Jameson [13] interpreted the relaxation as a pseudo-time dimension, using explicit time stepping to perform the relaxation. This ACM approach has also been extended to handle incompressible varying density flows, such as stratified flows [14,15]. More recently, Nishikawa [16] proposed a general technique where diffusion terms are hyperbolised. This has the advantage of stability scaling with h^{-1} — rather than h^{-2} — for some mesh spacing h. This approach fits naturally with ACM and has previously been investigated by Ahn [17] and Trojak et al. [18], who introduced novel techniques to optimise the computational implementation of ACM with hyperbolised diffusion (ACM-HD).

A major issue with ACM is the requirement to converge the pressure and velocity field for each time step, which can be costly, although some convergence acceleration methods have proved successful [19,20]. An alternative is the entropically damped artificial compressibility (EDAC) method introduced by Clausen [21]. Here entropy is not fixed, but density fluctuations are minimised. This results in a similar system of equations as ACM, with the primary difference being a pressure diffusion term. This approximation leads to time dependent equations which produce an almost divergence free flows thus enabling explicit time stepping to be used. Further studies have shown the method is effective on both model and real-world problems [22–24].

The aim of this paper is to compare and contrast three approaches for viscous incompressible flows, namely: ACM, ACM-HD, and EDAC. The focus of the investigation will be on the effect of parameterisation on accuracy and stiffness of the underlying systems. A specific objective is to understand if the explicit EDAC approach is more efficient when simulating incompressible flows compared to ACM or ACM-HD, and if so what effect, if any, is there on the flow field. Secondarily, to the authors knowledge the EDAC system has not previously been used with the FR approach and we wish to understand its effectiveness and the effect of varying the compressibility parameter within a high-order approach. Furthermore, as the EDAC system will be applied as a conservative equation, we wish to further the understanding of the Riemann problem as it forms an important part of the FR method [25].

To this end, in Section 2 we introduce the high-order FR approach used in this work. In Section 3, we detail the systems of governing equation for incompressible flow and the artificial compressibility approaches studied in this work. We also explore aspects of the eigenstructure of these equations. Some additional details on the Riemann problem are included in Appendices A and B. Then, in Section 4, the main numerical results on unsteady turbulent test cases are presented. Finally, conclusions are drawn in Section 5.

2. Preliminaries

In this work we consider artificial compressibility approaches solved via the high-order method flux reconstruction (FR) [5], as implemented in the PyFR solver [6]. The original FR method of Huynh [5] has been adapted to handle problems including advection–diffusion equations on element typologies such as simplicies, hypercubes, prisms, and affine pyramids. For completeness the FR method is summarised here, where for brevity we restrict the statement of the method to one dimension. [26,27] and references therein are recommended for applications to alternative topologies.

Characteristic of finite element methods, FR uses a partition of the domain K into N conformal sub-domains such that $K = \cup_{i=1}^{N} K_i$ and $K_i \cap K_j = \emptyset$ if $i \neq j$. Within each sub-domain, a number of nodes are positioned such that a Lagrange finite element can be formed for a conservation equation of the form

$$\begin{aligned} &\frac{\partial u}{\partial t} + \frac{\partial f}{\partial x} = 0, \quad \text{for} \quad u(x,t) : K \times \mathbb{R}_+ \mapsto U \subset \mathbb{R} \quad \text{and} \\ &f : U \mapsto \mathbb{R}, \quad \text{with} \quad u(x,0) = u_0(x), \end{aligned} \tag{1}$$

where in this description of FR we will assume K is periodic. It is typical to use a reference domain $\hat{K}$ with the projection $T_i : K_i \mapsto \hat{K}$ as this makes all the operators the same for a given element topology which has some clear computational benefits. For a line, quadrilateral, or hexahedral element a common choice of reference domain is: $\hat{K} = [-1,1]$, $\hat{K} = [-1,1]^2$, or $\hat{K} = [-1,1]^3$ respectively.

For the sub-domain K_i and points $x_{ij} \in K_i$, a Lagrange finite element can be formed giving the solution and flux polynomials as:

$$\hat{u}_i^{\delta} = \sum_{j=1}^{n_s} u_i(x_{ij}) l_j(r) \quad \text{and} \quad \hat{f}_i^{\delta} = \sum_{j=1}^{n_s} f(u_i(x_{ij})) l_j(r), \quad \text{for} \quad r \in \hat{K}, \tag{2}$$

where n_s is the number of nodal value within each element, and l_j is the jth Lagrange polynomial defined as

$$l_j(\xi) = \prod_{\substack{k=1 \\ k \neq j}}^{n_s} \frac{r - r_k}{r_j - r_k}, \tag{3}$$

for the set of reference points $\{r_1, \ldots, r_{n_s}\} \in \hat{K}$. In Eq. (2), $\hat{\bullet}$ symbolises this is in the reference domain and δ indicates this corresponds to a piece-wise discontinuous approximation. The flux reconstruction algorithm provides a method to calculate the gradient of the flux function, f, corresponding to a C^0 approximation of f in K. This gradient approximation is given as

$$\frac{\partial f_i}{\partial x} \approx \left(\frac{\mathrm{d}T_i}{\mathrm{d}r}\right)^{-1} \left(\frac{\mathrm{d}\hat{f}^{\delta}}{\mathrm{d}r} + \left(f_L^I - f_L^{\delta}\right) \frac{\mathrm{d}h_L}{\mathrm{d}r} + \left(f_R^I - f_R^{\delta}\right) \frac{\mathrm{d}h_R}{\mathrm{d}r} \right), \tag{4}$$

where $\bullet_L$ and $\bullet_R$ are the projection to the left and right interfaces. Then f_L^I is the common interface value formed by using $u_{i,L}^{\delta}$ and $u_{i-1,R}^{\delta}$ and similarly for f_R^I. Some degree of upwinding should be applied when calculating the common inviscid interface flux in order to stabilise the method. This may be provided from one of a number of approximate Riemann solvers [28]. These common interface values are applied to the element via polynomial correction functions $h_L(r)$ and $h_R(r)$. To enforce the common value, these functions have the conditions that $h_L(-1) = h_R(1) = 1$ and $h_L(1) = h_R(-1) = 0$.

Once the approximate flux divergence is calculated, one of a number of ODE integration techniques can be used. In this work, Runge–Kutta (RK) time integration will be used for explicit time stepping. When solving the dual time systems that arise in the ACM system, it is logical to use an implicit time scheme. In this case, the BDF2 method is used, coupled to an explicit RK smoother in pseudo-time. Throughout this work, we will use the adaptive low storage RK procedure of Kennedy et al. [29], specifically the RK3(2)4[2R+] method. This is a third order, four stage method where the embedded scheme is second order. The embedded system is used to predict the error [30] and a PI controller can be used to set either a global or local time step [19,27] for the physical time step or pseudo-time step, respectively.

3. Governing equations

3.1. Incompressible flow

The incompressible Navier–Stokes equations for a single phase and constant density can be written as:

$$\frac{\partial \mathbf{V}}{\partial t} + \mathbf{V}\cdot\nabla\mathbf{V} + \nabla P = \nu\nabla^2\mathbf{V} \quad \text{and} \quad \nabla\cdot\mathbf{V} = 0, \tag{5}$$

where $\mathbf{V} = [u, v, w]^T$ is the velocity vector, P is the pressure, and ν is the kinematic viscosity. Taking the divergence of this equation and enforcing a solenoidal velocity field gives the pressure Poisson equation

$$\nabla^2 P = -\nabla\cdot(\mathbf{V}\cdot\nabla\mathbf{V}). \tag{6}$$

This equation gives a closed form for pressure up to a constant offset. The difficulty arises from the global nature of solutions to the Poisson equation and the complexities of solving this in parallel with the same efficiency as hyperbolic and parabolic equations.

3.2. Artificial compressibility

The artificial compressibility method (ACM) introduced by Chorin [11] can be derived by starting from the compressible Navier–Stokes equations and imposing constant entropy to close an incompressible model [21]. A pseudo-time derivative can be introduced, which interprets a physical time step as converging the field variables in pseudo-time to a steady state. Here we will use τ for the pseudo-time dimension and t for the physical time dimension. This ACM system of equations can be written in conservative form as:

$$\begin{aligned}\frac{\partial}{\partial t}\begin{bmatrix}0\\u\\v\\w\end{bmatrix} + \frac{\partial}{\partial \tau}\begin{bmatrix}P\\u\\v\\w\end{bmatrix} + \nabla\cdot\begin{bmatrix}\zeta u & \zeta v & \zeta w\\ u^2+P & uv & uw\\ uv & v^2+P & vw\\ uw & vw & w^2+P\end{bmatrix}\\ = \nu\begin{bmatrix}0 & 0 & 0\\ \partial_{xx}u & \partial_{yy}u & \partial_{zz}u\\ \partial_{xx}v & \partial_{yy}v & \partial_{zz}v\\ \partial_{xx}w & \partial_{yy}w & \partial_{zz}w\end{bmatrix},\end{aligned} \tag{7}$$

where a compact notation for partial derivatives is used, for example $\partial_{xx}u = \frac{\partial}{\partial x}\frac{\partial u}{\partial x}$. Here, ζ is a measure of the compressibility of the flow in pseudo-time, defining an artificial Mach number of the flow as $M = \sqrt{1/\zeta}$. This governing equation shows that velocity divergence is balanced by pressure gradients in the pseudo-time dimension, with the key behaviour for incompressible flow that as $\partial_\tau P \to 0$ the velocity field converges on to a divergence free solution $\nabla\cdot\mathbf{V} \to 0$. Importantly though there is no explicit elliptic equation to solve, and a solver developed for conservation equations may be readily applied to ACM.

To understand how ζ effects stiffness and ultimately the propagation of information in the system, consider the flux vector in x is defined as $\mathbf{f} = [\zeta u, u^2 + P, uv, uw]^T$, then the inviscid flux Jacobian is given by:

$$\frac{\partial \mathbf{f}}{\partial \mathbf{U}} = \begin{bmatrix}0 & \zeta & 0 & 0\\ 1 & 2u & 0 & 0\\ 0 & v & u & 0\\ 0 & w & 0 & u\end{bmatrix}, \tag{8}$$

where $\mathbf{U} = [P, u, v, w]^T$. This is used to highlight the difference between the conserved variables in pseudo-time and real-time. The eigenvalue of this Jacobian can be found to be:

$$\lambda_1 = \lambda_2 = u, \quad \lambda_3 = u - a, \quad \text{and} \quad \lambda_4 = u + a, \tag{9}$$

for $a^2 = u^2 + \zeta$. The repeated eigenvalue indicates that the inviscid system is linearly degenerate, and through calculation of the eigenvectors, it can be seen that this results in a contact discontinuity in the Riemann problem with discontinuities in the tangential velocity components, v and w. As the contact is not stationary, exact or structure approximating Riemann solvers can be developed without complication via approaches such as that of Elsworth and Toro [31]. However, in this work only Rusanov approximate Riemann solvers were applied to give a common interface flux via:

$$\mathbf{f}^I = \frac{1}{2}\left(\mathbf{f}_L + \mathbf{f}_R\right) - \frac{1}{2}S_{\max}\left(\mathbf{U}_R - \mathbf{U}_L\right), \tag{10}$$

where the Davis type maximum wavespeed estimate is used as:

$$S_{\max} = \max\left(|u_L| + a_L, |u_R| + a_R\right). \tag{11}$$

Importantly this shows that the maximum absolute eigenvalue scales with $\sqrt{\zeta}$, i.e., the stiffness will scale with one over the fictional Mach number.

3.3. Artificial compressibility — Hyperbolised diffusion

The hyperbolic diffusion method of Nishikawa [16] aims to remove parabolic terms in governing equations through additional auxiliary equations which, once converged, yield the gradients of the conserved variables. As an example consider the linear advection–diffusion equation:

$$\frac{\partial \phi}{\partial t} + \frac{\partial \phi}{\partial x} = \nu\frac{\partial^2\phi}{\partial x^2},$$

the diffusion term can be hyperbolised by adding an auxiliary equation to give the system:

$$\begin{aligned}\frac{\partial \phi}{\partial t} + \frac{\partial \phi}{\partial \tau} + \frac{\partial}{\partial x}(\phi - \nu\psi) = 0,\\ \frac{\partial \psi}{\partial \tau} + \frac{\partial}{\partial x}\left(-\frac{\phi}{T}\right) = -\frac{\psi}{T}.\end{aligned}$$

Here pseudo-time is again used to converge the system, where T is a preconditioning parameter to account for the differing stiffness of the equations. This system can be understood by considering $\partial_\tau\psi \to 0$, as this happens $\psi \to \partial_x\phi$.

As the hyperbolic diffusion method and the artificial compressibility method can both be formulated to use pseudo-transient continuation, ACM is a good candidate for hyperbolic diffusion. The new ACM-HD governing conservation equations can then be expressed in three dimensions as:

$$\frac{\partial}{\partial t}\begin{bmatrix}0\\\mathbf{V}\\\mathbf{0}\\\mathbf{0}\\\mathbf{0}\end{bmatrix} + \frac{\partial}{\partial \tau}\begin{bmatrix}P\\\mathbf{V}\\\mathbf{q}\\\mathbf{r}\\\mathbf{s}\end{bmatrix} + \nabla\cdot\begin{bmatrix}\zeta\mathbf{V}^T\\ \mathbf{V}\otimes\mathbf{V} + P\mathbf{I} - \nu\mathbf{S}^T\\ -\frac{1}{T}\mathbf{V}\otimes\mathbf{I}\end{bmatrix} = -\frac{1}{T}\begin{bmatrix}0\\\mathbf{0}\\\mathbf{q}\\\mathbf{r}\\\mathbf{s}\end{bmatrix}, \tag{13}$$

where $\mathbf{V} = [u, v, w]^T$ and $\mathbf{I}$ is the identity matrix. Additionally, we have the vectors $\mathbf{q}$, $\mathbf{r}$, and $\mathbf{s}$, and the matrix $\mathbf{S} = [\mathbf{q}, \mathbf{r}, \mathbf{s}]$. These vectors will form the gradient of u, v, and w, respectively such that once converged $\mathbf{q} \to [\partial_x u, \partial_y u, \dots]^T$, $\mathbf{r} \to [\partial_x v, \dots]^T$, and $\mathbf{s} \to [\partial_x w, \dots]^T$.

The resulting Jacobian matrices, to the authors knowledge, have not been well analysed in the literature. The effect of hyperbolising diffusion on the stiffness can be seen when considering the Jacobian of the inviscid flux in the x direction (see the equation in Box I).
This yields the eigenvalues:

$$\begin{aligned}&\lambda_1 = \dots = \lambda_7 = 0, \quad \lambda_8 = \lambda_9 = \frac{u}{2} - c, \quad \lambda_{10} = \lambda_{11} = \frac{u}{2} + c,\\ &\lambda_{12} = u - b, \quad \lambda_{13} = u + b,\end{aligned} \tag{15}$$

where we use the definitions

$$b^2 = u^2 + \zeta + \frac{\nu}{T} \quad \text{and} \quad c^2 = \frac{u^2}{4} + \frac{\nu}{T}. \tag{16}$$

Consequently, a Davis estimate of the maximum absolute eigenvalue can be taken as:

$$S_{\max} = \max\left(|u_L| + b_L, |u_R| + b_R\right). \tag{17}$$

$$\frac{\partial \mathbf{f}}{\partial \mathbf{U}} = \begin{bmatrix} 0 & \zeta & 0 & 0 & 0 & 0 & 0 & 0 & 0 & 0 & 0 & 0 & 0 \\ 1 & 2u & 0 & 0 & -\nu & 0 & 0 & 0 & 0 & 0 & 0 & 0 & 0 \\ 0 & v & u & 0 & 0 & 0 & 0 & -\nu & 0 & 0 & 0 & 0 & 0 \\ 0 & w & 0 & u & 0 & 0 & 0 & 0 & 0 & 0 & -\nu & 0 & 0 \\ 0 & -1/T & 0 & 0 & & & & & & & & & \\ 0 & 0 & 0 & 0 & & & & & & & & & \\ 0 & 0 & 0 & 0 & & & & & & & & & \\ 0 & 0 & -1/T & 0 & & & & & & & & & \\ 0 & 0 & 0 & 0 & & & & & \mathbf{0} & & & & \\ 0 & 0 & 0 & 0 & & & & & & & & & \\ 0 & 0 & 0 & -1/T & & & & & & & & & \\ 0 & 0 & 0 & 0 & & & & & & & & & \\ 0 & 0 & 0 & 0 & & & & & & & & & \end{bmatrix}. \tag{14}$$

Box I.

Giving consideration to how the preconditioning parameter, T, is set, if $T = \mathcal{O}(\nu)$ is used then the stiffness will be approximately independent of the viscosity. An alternative argument was been proposed by Nishikawa and Liu [32] where $T = \mathcal{O}(1/\nu)$, which results in convergence independent of ν.

From the analysis above, we see that the system has several repeated eigenvalues, highlighting another feature of this governing equation, there will be a linear degeneracy in the Riemann problem; in this case resulting in a stationary contact discontinuity. This introduces poses a difficulty in formulating an exact Riemann solver or an HLLC type approximate solver to produce the common interface flux, as a fully resolved problem would have a contact discontinuity at the interface. The alternative is to again use a Rusanov type Riemann approximate solver with Davis wavespeed estimate for $[P, u, v, w]^T$. Central differencing was used for the remaining terms owing to the diffusive nature of the auxiliary equations. More details of the Riemann problem relating to ACM-HD are given in Appendix A.

An advantage of this system is that it solely has first order derivatives in the system and consequently the numerical stability is only dependent on the advection scheme, which scales with h^{-1}. The cost of solving several additional equations can be ameliorate by the unique optimisation opportunities when solving a purely advective system [18], as well as the increased rate of convergence reported for hyperbolic diffusion [32].

3.4. Entropically damped artificial compressibility

Clausen [21] introduced the entropically damped artificial compressibility (EDAC) method where closure was achieved by minimising density variations, rather than constant entropy as in ACM. This leads to the following evolution equation for pressure

$$\frac{\partial P}{\partial t} + \mathbf{V} \cdot \nabla P + \frac{1}{M^2} \nabla \cdot \mathbf{V} = \frac{1}{Re} \nabla^2 P, \tag{18}$$

where Re is a Reynolds number. The key difference is that parabolic regularisation introduced to the mass equation removes the need for pseudo-transient continuation, i.e. explicit time stepping can be used. The name EDAC then stems from the relationship between pressure diffusion and entropy. If entropy is defined via the functional $\sigma = \log(P)$, then pressure diffusion terms will provide damping to the entropy field. To see this consider the companion entropy equation which may be calculated explicitly, following the general form of Dafermos [33], for the entropy–flux pair $(\sigma, \boldsymbol{\Sigma}) = (\log(P), \mathbf{V}\sigma)$:

$$\frac{\partial \sigma}{\partial t} + \nabla \cdot \boldsymbol{\Sigma} = \frac{1}{Re P} \nabla^2 P. \tag{19}$$

Not only does this show how pressure diffusion effects the entropy, but it also shows that areas of low pressures will move the solution away from the physical condition of constant entropy if accompanied by a second derivative of pressure. For example, the canonical case of laminar flow around a cylinder.

In order to apply the EDAC method in the PyFR framework, it must be cast as a conservation law. If it is assumed that $\nabla \cdot \mathbf{V} = 0$, then in three-dimensions we obtain

$$\mathbf{Q} = \begin{bmatrix} P \\ u \\ v \\ w \end{bmatrix}, \quad \mathbf{F}^{\text{inv}} = \begin{bmatrix} u(P+\zeta) & v(P+\zeta) & w(P+\zeta) \\ u^2 + P & uv & uw \\ uv & v^2 + P & vw \\ uw & vw & w^2 + P \end{bmatrix}, \quad \text{and} \quad \mathbf{F}^{\text{vis}} = \nu \begin{bmatrix} \partial_x P & \partial_y P & \partial_z P \\ \partial_x u & \partial_y u & \partial_z u \\ \partial_x v & \partial_y v & \partial_z v \\ \partial_x w & \partial_y w & \partial_z w \end{bmatrix}, \tag{20}$$

for

$$\partial_t \mathbf{Q} + \nabla \cdot \mathbf{F}^{\text{inv}} = \nabla \cdot \mathbf{F}^{\text{vis}}, \tag{21}$$

where $1/M^2 = \zeta$ and $1/Re = \nu$. This formulation shows a second aspect of EDAC, that pressure fluctuations are resolved spatially whereas in ACM they could be resolved in pseudo-time.

To understand how the propagation of information differs in this system, we will again consider the inviscid flux Jacobian in x, $\mathbf{f} = \mathbf{F}^{\text{inv}} \cdot [1, 0, 0]^T$:

$$\frac{\partial \mathbf{f}}{\partial \mathbf{Q}} = \begin{bmatrix} u & P+\zeta & 0 & 0 \\ 1 & 2u & 0 & 0 \\ 0 & v & u & 0 \\ 0 & w & 0 & u \end{bmatrix}, \tag{22}$$

then the eigenvalues can be found to be:

$$\lambda_1 = \lambda_2 = u, \quad \lambda_3 = \frac{3}{2}u - d, \quad \text{and} \quad \lambda_4 = \frac{3}{2}u + d, \tag{23}$$

for $d^2 = u^2/4 + P + \zeta$. A Davis estimate may again be constructed as:

$$S_{\max} = \max\left(\frac{3}{2}|u_L| + d_L, \frac{3}{2}|u_R| + d_R\right). \tag{24}$$

Having defined these speeds, we will mainly use the Rusanov approximate Riemann solver throughout this work for EDAC. However, in Appendix B we explore the Riemann problem in more detail and define an HLLC approach which will also be investigated numerically. A further insight given from Appendix B is that the EDAC system cannot support a Riemann problem which leads to a solution containing two rarefaction waves. Although the concept of a shock in an artificial compressibility system is strange, this property can be thought of as consistent with the entropy dissipation of the method.

Comparison of these eigenvalues to ACM shows a new pressure dependency which is interpreted as a consequence of resolving velocity

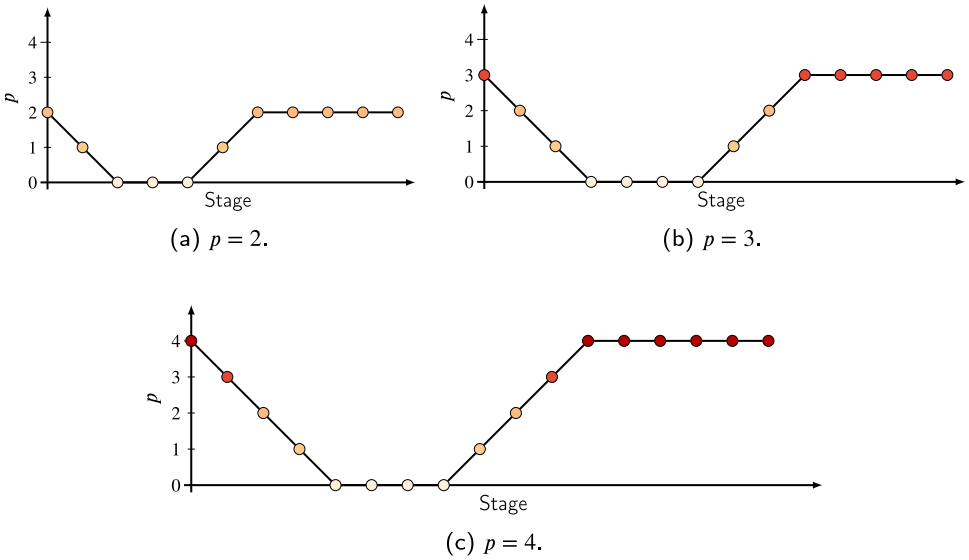

Fig. 1. P-multigrid cycles used for various orders.

divergence as pressure waves in space. Furthermore, assuming that $S_{\max}$ scales with the true maximum absolute eigenvalue, it can be seen that the EDAC system will often be significantly stiffer and, given that the permitted the use of explicit time stepping, this could lead to smaller stable time steps.

4. Numerical experiments

4.1. TGV at $Re = 1600$

The Taylor–Green [34] vortex is a well studied test case which exhibits three regimes: an inviscid laminar regime, turbulent transition through vortex sheet roll-up, and full homogeneous isotropic turbulent decay. The last regime is generally observed for $Re \gtrsim 1000$ [35]. The initial condition is taken as:

$$P = \frac{1}{\gamma M^2} + \frac{1}{16}\cos(2z+2)\left[\cos(2x) + \cos(2y)\right], \tag{25a}$$

$$u = \sin x \cos y \cos z, \tag{25b}$$

$$v = -\cos x \sin y \cos z, \tag{25c}$$

$$w = 0, \tag{25d}$$

where a typical Mach number is $M = 0.08$. When performing ACM-HD calculations, these terms are differentiated to give the initial gradients. The domain is a fully periodic cube $\Omega = [0, 2\pi]^3$, which was partitioned into a mesh of regular hexahedral elements with approximately 128^3 solution points depending on order. The solution and flux point locations in the reference domain were set using the tensor product of the Gauss–Legendre quadrature. For this case, unless otherwise stated, the common inviscid flux is calculated using a Rusanov type approach as detailed in Section 3. For the ACM and EDAC methods, the common viscous interface flux in calculated using an LDG approach with a small penalty, $\epsilon = 0.1$. Two separate time integration schemes were used. For ACM and ACM-HD, BDF2 was coupled to an adaptive RK34 explicit smoother, details of which can be found in Section 2. This same RK method was used for the explicit time stepping of the EDAC method; however, with global adaptation of the explicit physical step rather than locally for the pseudo stepping. To further accelerate the convergence of the ACM and ACM-HD calculations, P-multigrid was used [36]. The cycles used are shown in Fig. 1 as they were found to give rapid convergence and follow the suggested asymmetry of Trojak and Witherden [37]. The exact configuration files can be found in the attached electronic supplementary material.

Several functionals were used to access the numerical performance of the AC methods. The first is enstrophy, defined as:

$$\epsilon(t) = \frac{\nu}{|\Omega|}\int_\Omega \boldsymbol{\omega}(t,\mathbf{x})\cdot\boldsymbol{\omega}(t,\mathbf{x})\,\mathrm{d}\mathbf{x}, \tag{26}$$

where the vorticity is defined as $\boldsymbol{\omega} = \nabla \times \mathbf{V}$. Reference DNS data for this functional was provided by Van Rees in private communication, containing results for a longer time period than that detailed in van Rees et al. [38]. Two further functionals were examined to assess the quality of the incompressible solution:

$$s_s(t) = \frac{1}{|\Omega|}\int_\Omega \nabla\cdot\mathbf{V}(t,\mathbf{x})\,\mathrm{d}\mathbf{x} \quad \text{and} \quad s_a(t) = \frac{1}{|\Omega|}\int_\Omega |\nabla\cdot\mathbf{V}(t,\mathbf{x})|\,\mathrm{d}\mathbf{x}. \tag{27}$$

These are the volume averaged velocity divergence and absolute velocity divergence.

In order to evaluate the EDAC method, a sweep was performed for $\zeta \in \{3, \ldots, 100\}$ at orders 2, 3, and 4. Studying Fig. 2, it can be observed that ζ does not have a significant effect on the enstrophy production for the EDAC method at this resolution, and the largest differences are seen at the peak dissipation. Comparison is made in Fig. 3(a) between EDAC and the other ACM methods. This shows that after peak enstrophy production, there is a noticeable deviation between the results. A further comparison can be made from Fig. 3 between EDAC and the compressible Navier–Stokes equations (NSE) at $M = 0.08$. This makes it clear that EDAC and NSE are comparable, caused by both methods dissipating entropy due to compressibility and both systems having a similar Mach number. In contrast, the ACM and ACM-HD systems do not cause entropy dissipation and the results are evidently different from the entropically damped systems. There is also a notable disparity between the ACM and ACM-HD systems at $p = 2$. The difference is due to Eq. (26) being evaluated with the converged gradient terms in ACM-HD, which are one order higher than the reconstructed gradients used in standard ACM. This difference is more notable at lower p as the polynomial space is more restricted.

Fig. 4 presents the time averaged values of s_a against $\sqrt{\zeta}$. For EDAC, Fig. 4(a), a linear relation between the time averaged $\overline{s_a}$ and $\sqrt{\zeta}$ is observed at high ζ. Furthermore, by comparison to the ACM results, the divergence of EDAC is approximately 1.5× lower. This linear relationship is not observed for ACM and ACM-HD. Instead, the benefit of increasing ζ is diminishing. For the dual time stepping of ACM and ACM-HD, a constant $\Delta t = 0.01$ and locally adaptive $\Delta\tau$ with initial value of 0.0025 was used for all runs. For this configuration at $p = 4$, $\zeta > 5.2$ was unstable with ACM and $\zeta > 6.6$ for ACM-HD. From the data presented in Figs. 4(b) and 4(c), all configurations tested for ACM-HD

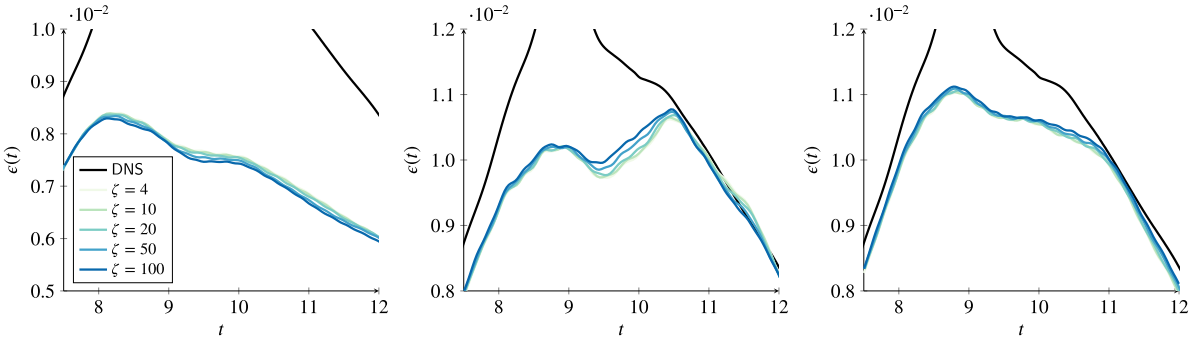

(a) EDAC, $p = 2$. (b) EDAC, $p = 3$. (c) EDAC, $p = 4$.

Fig. 2. Taylor–Green vortex enstrophy comparison for DoF $\approx 128^3$. DNS data courtesy of van Rees, private communication.

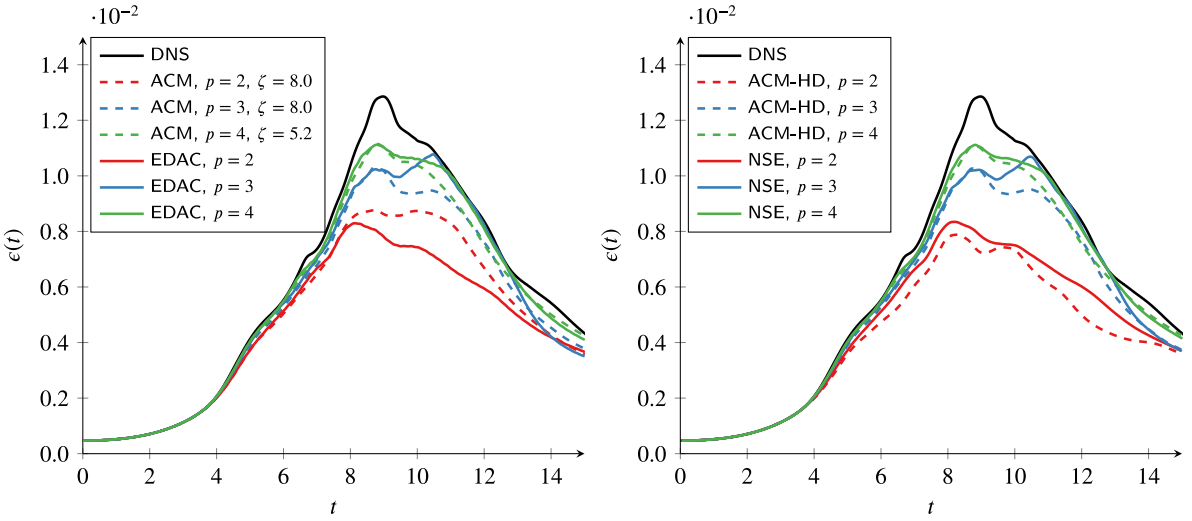

(a) ACM and EDAC, here $\zeta = 100$ is used for EDAC. (b) NSE and ACM-HD, here $T = 10\nu$ and ζ is 8.0, 8.0, and 6.6, for order 2,3, and 4 respectively for ACM-HD.

Fig. 3. Comparison of TGV $\epsilon(t)$ with $\sim 128^3$ DoF for various schemes and orders.

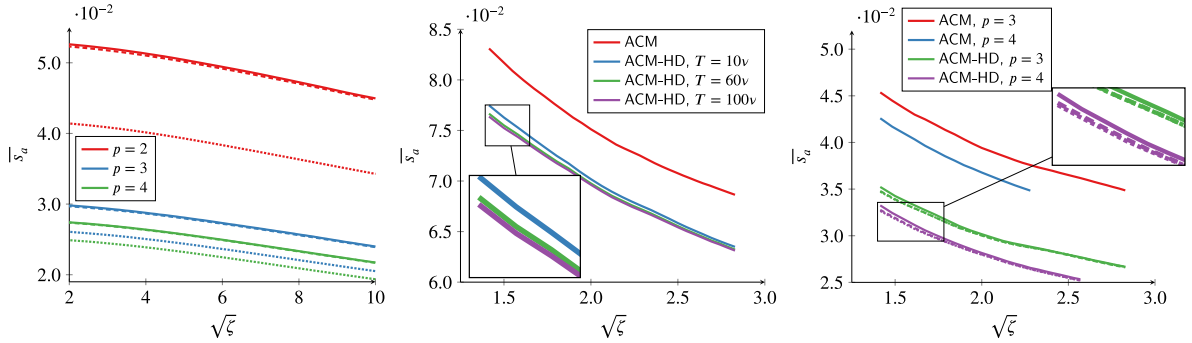

(a) EDAC, solid: Rusanov, dashed: HLL, dotted: HLLC. (b) ACM and ACM-HD, $p = 2$ (c) ACM and ACM-HD, $p = 3$ and $p = 4$, solid: $T = 10\nu$, dashed: $T = 60\nu$, dotted: $T = 100\nu$.

Fig. 4. Variation of the TGV mean absolute divergence integral with $\sqrt{\zeta}$. Averaged over $t \in [0, 15]$.

led to lower velocity divergence than ACM, which is attributable to the improved convergence properties of hyperbolic diffusion methods. Furthermore, lower values of T could lead to lower values of velocity divergence, but as ζ increased, this effect diminished. This is indicative of the increased stiffness in the mass equation leading to it becoming dominant in the convergence of the system.

An interesting phenomenon is observed in Fig. 5(a) for EDAC. Here, after peak dissipation, the ratio of absolute divergence to enstrophy becomes approximately linear. Outside of the enstrophy production regime, the source of this can be understood from the vorticity form of the momentum equation. A term that scales with both vorticity and velocity divergence, that would ordinarily cancel, is present in the

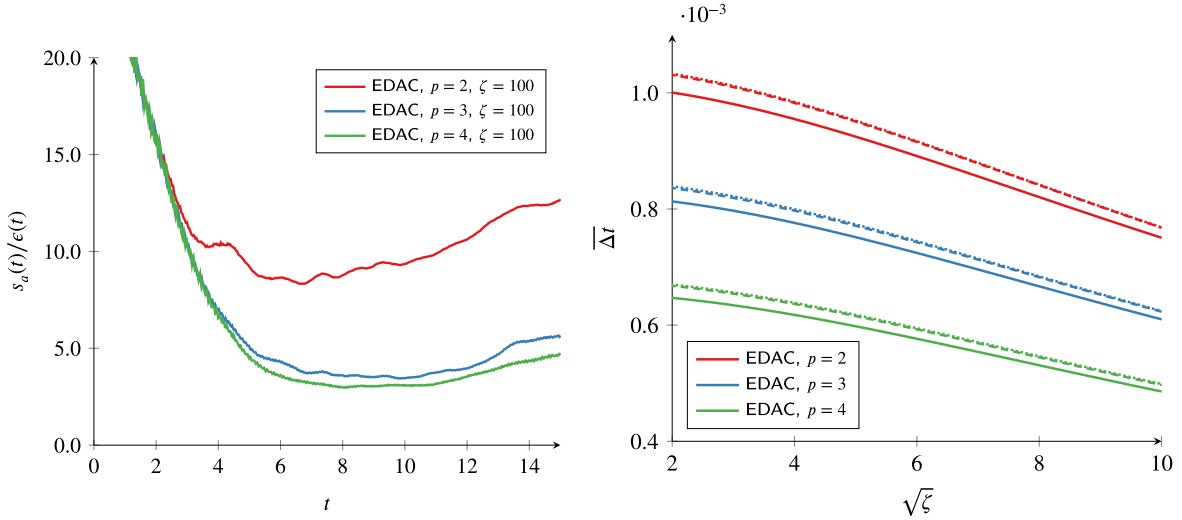

(a) Evolution of the ratio of absolute divergence to enstrophy in the TGV. Here a 20 point moving average is applied to s_a.

(b) Average Δt for the the TGV using EDAC, solid: Rusanov, dashed: HLL, dotted: HLLC.

Fig. 5. Error and average time step size evolution for the TGV when solved using the EDAC method.

vorticity equation. The conclusion, which may have been anticipated, is that vortex dominated flows may induce stronger divergence clearing from the method, which may in turn be problematic for EDAC as this manifests as larger pressure fluctuations. At lower order, due to lower enstrophy production and higher numerical dissipation, this relationship is not as clear.

In several places we have considered the maximum eigenvalue due to its importance in the efficacy of the explicit Runge–Kutta time integration. A lower absolute maximum eigenvalue will increase the maximum stable time step, but clearly from Section 3.4 increasing ζ will increase the maximum absolute eigenvalue. Therefore, a trade-off between stiffness, runtime and divergence, exists.

For the EDAC method, a globally adaptive time stepping procedure was used. To understand the trade-off that occurs, the statistics of the time steps used were collected and the average time step size is shown in Fig. 5(b). This shows the same linear relationship at high $\sqrt{\zeta}$ values as was observed for the divergence. In the case of Δt, the origin of this relationship can be clearly seen form the eigenvalues of the inviscid flux for the EDAC system of equation. In Figs. 4(a) and 5(b) results are also presented for HLL and HLLC as well as Rusanov. The HLL and HLLC schemes are derived in Appendix B. These data show that HLLC can give a sizeable reduction in the divergence average, and both HLL and HLLC lead to an increase in the maximum usable Δt. The cause of this is a better model of the maximum stable eigenvalue, as the Davis wavespeed estimate more often over predicts this wavespeed [39], which will lead to a stricter CFL condition. Based on these results there is a clear benefit to using the HLLC Riemann solver at the interfaces, and given the availability of FLOPs on GPU, the additional computation can be largely hidden by memory latency caused by bandwidth limitations.

4.2. Circular cylinder at $Re = 3900$

The circular cylinder has previously been studied in great detail, a comprehensive review was presented by Williamson [40]. When $Re = 3900$, the flow is in a sub-critical regime and is considered to be both computationally challenging and physically interesting. This is due to the presence of multiple phenomena, namely: a laminar boundary-layer, separation, a free shear-layer, turbulent transition of the free shear-layer, and a turbulent wake. The difficulties in simulating this case are exemplified by the spread of reported drag coefficients in the literature [41], with a value in the range of $C_d \in [1, 1.4]$ being not uncommon. Subsequently reported by Lehmkuhl et al. [42], a cause for this is that the time averaged wake has two distinct modes, a low energy L-mode and a high energy H-mode, with long non-dimensional times separating transition event between the modes, typically of the order 10^3. Owing to this long time between transitions, a simulation will typically only capture a single mode.

In the work of Vermeire et al. [43] the PyFR solver was compared to other tools. It was shown that with an appropriate mesh simulations of the compressible Navier–Stokes equations at $M = 0.2$ gave good agreement with the DNS results of Lehmkuhl et al. [42]. For this reason we will use the same mesh in this investigation which covered the domain $\Omega = [-9D, 25D] \times [-9D, -9D] \times [0, \pi D]$ for diameter D. More recently, Dzanic et al. [44] performed a DNS of this case. Comparison is made later to their data, as well as to additional TKE budget data collected by the present authors rerunning their configuration.

For this test, seven configurations were tested: EDAC with $\zeta \in \{4, 20, 100\}$, ACM with $\zeta \in \{3, 4.5\}$ and ACM-HD $\zeta = 3$ with $T \in \{10\nu, 100\nu\}$. The case was set with a free-stream velocity and pressure of $U = 0.2\sqrt{\gamma}$ and $P_0 = 1$. Constant velocity inlet and constant pressure outlet boundary conditions were used for all cases. Although, Riemann invariant boundary conditions are available, they were deemed unnecessary in this case. An initialisation period was set from 0 to $\hat{t} = tU/D = 47$ at $p = 2$ followed by $p = 4$ until $\hat{t} = 100$. Afterwards, the time average statistics were collected until $\hat{t} = 200$. To accelerate the convergence of the ACM and ACM-HD dual time stepping, the same P-multigrid method was used as described in Section 4.1.

The instantaneous Q-criterion for the EDAC method at $\hat{t} = Ut/D = 201$ is shown in Fig. 6. Some differences in the wake structure are visible and notably at lower ζ values the free shear layer appears to transition earlier. Focusing on EDAC initially, the time and span averaged velocity profiles — Figs. 7 and 8 — show that there is a pronounced difference between the different ζ values, with the highest value of ζ giving the best agreement with the DNS H-mode. Notably as ζ is increased, monotonic convergence is not observed, although the Q-criterion plots indicate transition is delayed for $\zeta = 20$ compared to $\zeta = 4$. However, studying the wake smaller structures appear to have coalesced into larger scale structures, and additional comparison can be made with Q-criterion plots in Appendix C. Fig. 20 shows the power spectral density of span-wise and stream-wise velocity in the wake, where for all three configurations the same vortex shedding peak and Kelvin–Helmholtz peak were observed at $St \approx 0.4$ and $St \approx 3$ respectively.

(a) EDAC, $\zeta = 4$, $\hat{t} = 201$. (b) EDAC, $\zeta = 20$, $\hat{t} = 201$. (c) EDAC, $\zeta = 100$, $\hat{t} = 201$.

Fig. 6. Iso-contours of Q-criterion, $Q = 0.1$, coloured by velocity magnitude.

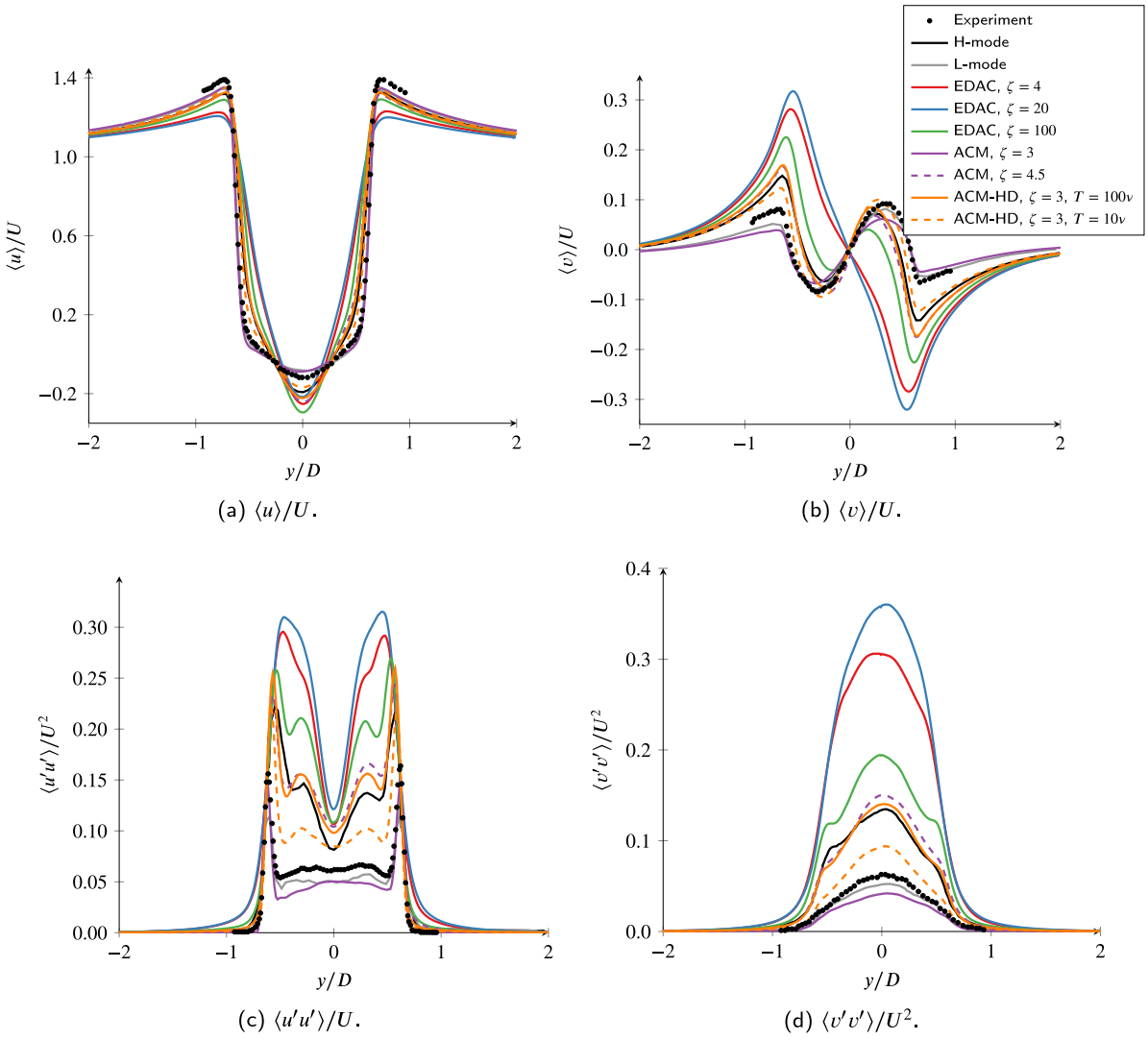

(a) $\langle u \rangle / U$. (b) $\langle v \rangle / U$.

(c) $\langle u'u' \rangle / U$. (d) $\langle v'v' \rangle / U^2$.

Fig. 7. $x/D = 1.06$, with experimental data from Parnaudeau et al. [45] and DNS data from Lehmkuhl et al. [42].

Studying the progression of the streamwise Reynolds stress through the downstream slices, Figs. 7(c) and 8(c), it is observed that EDAC initially overestimates the Reynolds stresses, leading to the downstream stresses at $x/D = 2.02$ being under-predicted. The results at $x/D = 1.56$ are shown in Fig. 19, and are similar to those at $x/D = 2.02$, implying the primary impact is to turbulent transition which occur further upstream. These differences observed will impact the turbulent kinetic energy budget, a detailed study of which is presented by Tian and Xiao [46] who showed that at $x/D = 1.06$, a balance exists between the convection, production, pressure transport, turbulent transport, and dissipation. Closer still to the cylinder, Tian and Xiao [46] showed the production term is dominant, and we hypothesise that over-production would lead to a downstream energy deficit, and that this is happening for EDAC. The turbulent production is defined as

$$\mathcal{P} = \langle u_i u_j \rangle \overline{S}_{ij}, \quad \text{and} \quad \overline{S}_{ij} = \frac{1}{2}\left(\frac{\partial \langle u_i \rangle}{\partial x_j} + \frac{\partial \langle u_j \rangle}{\partial x_i} \right), \tag{28}$$

where we have used Einstein notation.

Plotting the production term at $x/D = 1.06$, Fig. 9(a), over-production is clearly visible in comparison to DNS data. This is followed by a drop and subsequent under-prediction of production downstream, Fig. 9(c). From the average pressure profiles of Fig. 10 it can be seen that the pressure in the wake region is significantly lower than the DNS

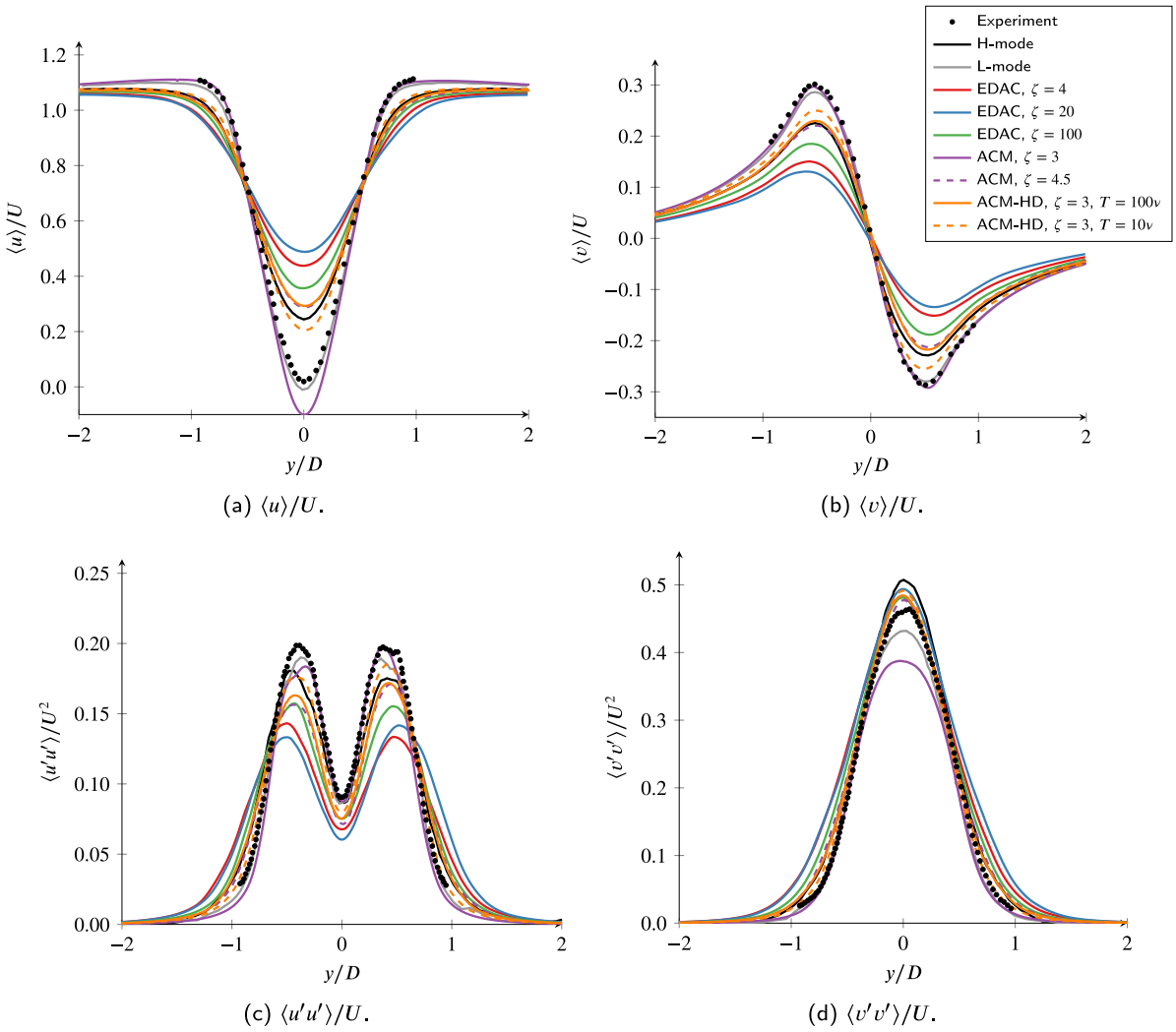

(a) $\langle u \rangle / U$. (b) $\langle v \rangle / U$.

(c) $\langle u'u' \rangle / U$. (d) $\langle v'v' \rangle / U$.

Fig. 8. $x/D = 2.02$, with experimental data from Parnaudeau et al. [45] and DNS data from Lehmkuhl et al. [42].

of Dzanic et al. [44]. This is a result of the artificial compressibility in the pressure field. From the interpretation that $\zeta = 1/M^2$, it can be understood that this pressure variation will increase as ζ decreases. This pressure gradient increases turbulent production through a balancing of shear and pressure in the momentum equations. Similarly as the pressure gradient reduces downstream, there is an associated drop in production. This highlights the difference between the EDAC method and ACM. In ACM, the velocity divergence is balanced by pressure fluctuations resolved in pseudo-time, whereas the EDAC method uses the alternative mechanism of spatial pressure variations. The spatial pressure fluctuation are able to have a significant impact on the observed physics, whereas in pseudo-time they are diffused and convected out of the solution by the explicit smoother. A further effect of the pressure reduction is an increase in the entropy dissipation, as seen from Eq. (26), which helps to explain the energy deficit.

Studying the ACM and ACM-HD results, it can be observed from Fig. 7 that the ACM simulation with $\zeta = 3$ is in the L shedding mode, whereas all the other results are in the H shedding mode. This highlights the sensitivity of this case and which mode is initially captured. For ACM-HD, it is observed that when $T = 100\nu$ the wake profiles are substantially more accurate than when $T = 10\nu$ and, given that a higher T reduces the stiffness while in the asymptotic limit, a higher T is preferred. The ACM results for $\zeta = 4.5$ are comparable to ACM-HD for $\zeta = 3$ and $T = 100\nu$. However, from the case setup, this ACM configuration was on the limit of what is stable. This can also be understood when considering the results of Fig. 4(c).

As was discussed in Section 4.1, the increased stiffness of the EDAC method at higher ζ values will lead to lower maximum stable time steps, in turn negatively impacting the runtime. The data in Table 1 gives a runtime comparison for one flow over diameter of the cylinder, from $\hat{t} = 201$ to $\hat{t} = 202$. This shows that increasing ζ by a factor of 5 gives approximately doubles the runtime of EDAC, which is approximately in line with the increase in the value of λ predicted from section Section 3.4. Furthermore, the runtimes for EDAC were observed to be lower than those of ACM; however, to achieve comparable results to ACM, ζ for EDAC would need to increased and is unlikely to be faster in that case. For the cylinder case with ACM it was found that $\Delta t = 2 \times 10^{-3}$ and $\Delta t / \Delta \tau = 20$ were stable, whereas due to the increased stability of ACM-HD $\Delta t = 4 \times 10^{-3}$ and $\Delta t / \Delta \tau = 20$ could be used. This is the cause of reduced runtime of ACM-HD compared to ACM observed in Table 1, and is one of the attractive features of hyperbolic diffusion. Although more equations are solved, the simpler advection algorithm coupled to the stability improvement lead to a speedup even at lower Reynolds numbers [18].

4.3. SD7003 at $Re = 6 \times 10^4$

The SD-7003 aerofoil [47] is an asymmetric aerofoil that has been explored in several studies, for example the studies by Beck et al. [48], Galbraith and Visbal [49], and Garmann et al. [50]. The configuration tested here is $Re = 6 \times 10^4$, at an angle-of-attack of $\alpha =$

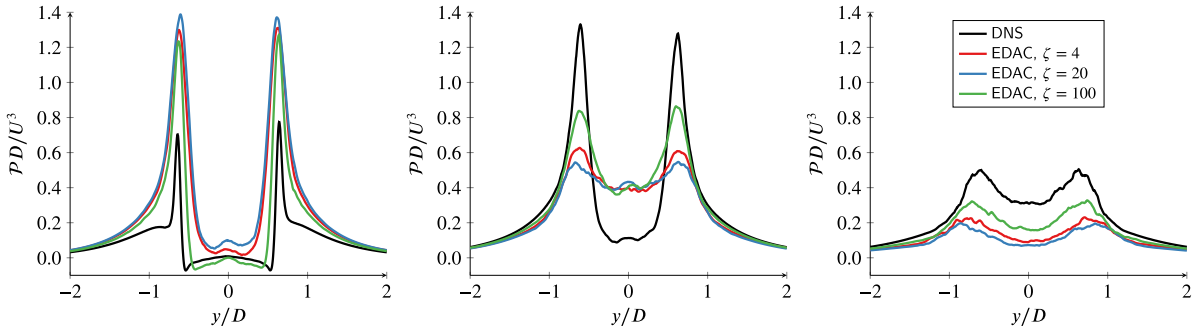

(a) $x/D = 1.06$. (b) $x/D = 1.54$. (c) $x/D = 2.02$.

Fig. 9. Span averaged turbulent production, $\mathcal{P}D/U^3$, for several downstream slices, DNS from Dzanic et al. [44].

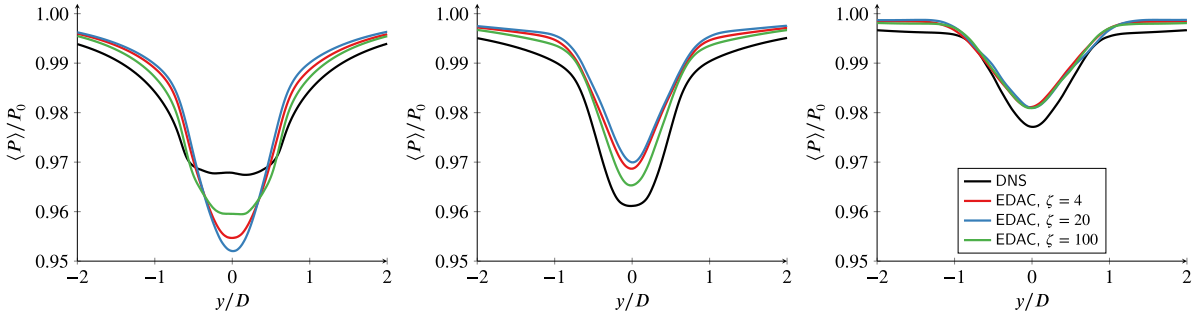

(a) $x/D = 1.06$. (b) $x/D = 1.54$. (c) $x/D = 2.02$.

Fig. 10. Span averaged pressure, $\langle P \rangle / P_0$, for several downstream slices, DNS from Dzanic et al. [44].

Table 1
Runtime for circular cylinder at $Re = 3900$ and $p = 4$ for one flow over diameter and 12 partitions run using NVIDIA V100 GPUs.

Scheme	Configuration	Wall time
ACM, $\zeta = 4.5$	RK3(2)4[2R+], PMG, LAPTS	0:32:14
ACM, $\zeta = 3$	RK3(2)4[2R+], PMG, LAPTS	0:31:55
ACM-HD, $\zeta = 3$, $T = 100\nu$	RK3(2)4[2R+], PMG, LAPTS	0:27:36
ACM-HD, $\zeta = 3$, $T = 10\nu$	RK3(2)4[2R+], PMG, LAPTS	0:22:29
EDAC, $\zeta = 100$	RK3(2)4[2R+], GAPTS	0:25:12
EDAC, $\zeta = 20$	RK3(2)4[2R+], GAPTS	0:12:18
EDAC, $\zeta = 4$	RK3(2)4[2R+], GAPTS	0:06:48

8°. In this configuration, a laminar separation bubble is formed on the suction surface followed by turbulent transition of the boundary layer. From numerical studies [48–50], it has been shown that the lift and drag coefficient are sensitive to the separation location, which in turn will be dependent on the surface pressure distribution. This configuration was previously used by Loppi et al. [19] to assess the effectiveness of locally adaptive pseudo-time stepping and P-multigrid in the convergence acceleration of ACM within the PyFR framework.

To allow direct comparison to the results of Loppi et al. [19], the same mesh was used in this investigation and was found to give good agreement with DNS data. The mesh is made up of 137 916 hexahedral elements covering a domain formed of a rectangular downwind section of $[0, 20c]\times[-10c, 10c]\times[0, 0.2c]$, with an upwind extruded semi-circle of diameter $20c$, where c is the chord length. The time integration method used here is again an explicit RK3(2)4[2R+] scheme with globally adaptive time stepping. The calculation was performed for $t \in [0, 60]$ with the divergence and global force metrics output periodically as well as data on the time step size used. As this case is at a higher Re, aliasing is of greater concern. To ameliorate this, over-integration anti-aliasing of the flux at the solution points is used [51]. All methods on this case were run at $p = 4$ and the over-integration order was set to $q = 11$, similar to the setup of Loppi et al. [19].

The effect of different ζ terms for the EDAC scheme can be qualitatively understood from the Q-criterion iso-surfaces shown in Fig. 11. These plots can be interpreted as showing a significantly thicker boundary layer in the $\zeta = 4$ case, as well as some variation in the transition point. Study the coefficient of lift and drag presented in Fig. 12, it is observed that $\zeta = 4$ significantly over-predicts drag and under-predicts lift, consistent with the boundary layer thickening observed in the instantaneous flow fields. At the higher values of ζ, good agreement is achieved in comparison to the numerical results of Vermeire et al. [43] and Loppi et al. [19]. Subjectively, the lower $\zeta = 20$ results are more similar to the compressible results of Vermeire et al. [43], whereas $\zeta = 100$ compares more favourably with the ACM results of Loppi et al. [19].

To understand the cause of the poor results at $\zeta = 4$, we investigated the time and span averaged stream-wise velocity and pressure at the trailing edge, shown in Fig. 14 and averaged over $\hat{t} \in [0, 60]$. No detailed DNS data for this particular configuration seem to be available; however, it is clear that there are significant differences in the physics observed. From Section 4.2 it was concluded that spatial pressure variations of EDAC are providing the mechanism driving the inaccuracy. Here, rather than early transition and over-production, Fig. 14(a) shows that there is recirculating region on the suction surface, indicative of a larger adverse pressure gradient. This recirculating flow is then responsible for a thicker boundary layer, which in turn will lead to higher C_d. As the thicker boundary layer will reduce the flow turning, this will also lower the C_l.

As was stated earlier, ζ can have a considerable effect on the stiffness of EDAC, Δt, and the runtime. The average Δt for different EDAC configurations applied to the SD7003 are presented in Table 2. Also included is the predicted increase in Δt using the approximate absolute eigenvalue based on the inflow and outflow conditions. This approximation under-predicts the impact of ζ; however, it does give a good first approximation if trying to predict simulation cost and is consistent with Fig. 5(b).

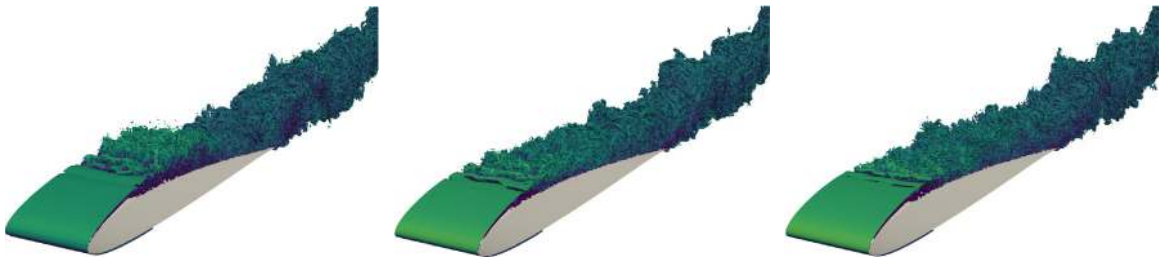

(a) EDAC, $\zeta = 4$, $\hat{t} = 47$. (b) EDAC, $\zeta = 20$, $\hat{t} = 47$. (c) EDAC, $\zeta = 100$, $\hat{t} = 47$.

Fig. 11. Iso-contours of Q-criterion, $Q = 20$, coloured by velocity magnitude for the SD7003 at $Re = 6 \times 10^4$ and $\alpha = 8°$.

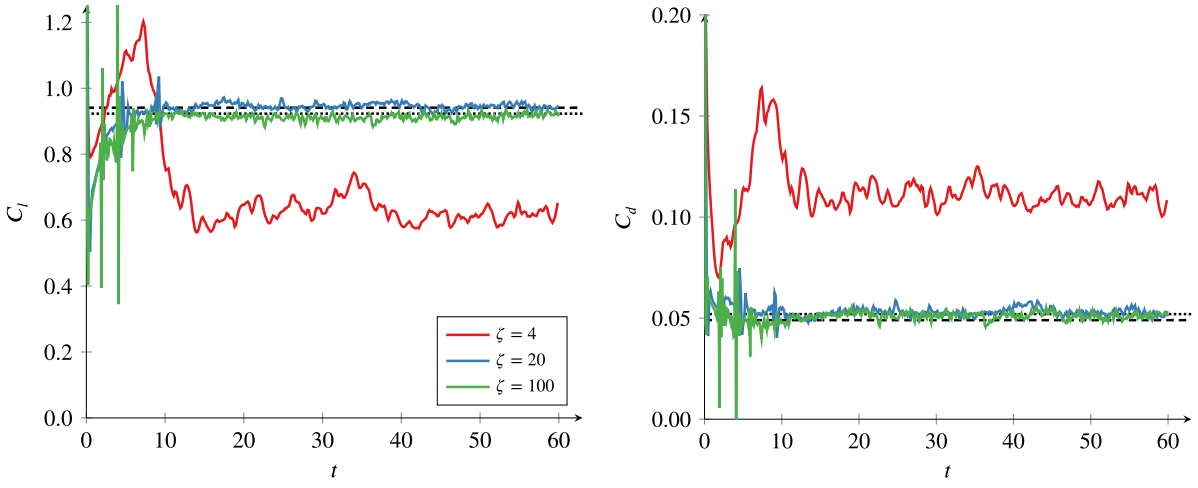

(a) Coefficient of Lift (b) Coefficient of Drag

Fig. 12. Coefficient of lift and drag, using FR, $p = 4$, for the SD7003 at $\alpha = 8°$ and $Re = 6 \times 10^4$. (dotted) data for ACM on the same mesh by Loppi et al. [19], (dashed) is data at $M = 0.2$ from Vermeire et al. [43].

Table 2
EDAC average time step size with RK34 for SD7003 case.

ζ	$\overline{\Delta t}$	$\overline{\Delta t}$ growth	Est. $\lambda_{\max}$ ratio
100	9.44×10^{-6}	–	–
20	1.88×10^{-5}	1.99	1.79
4	3.36×10^{-5}	1.79	1.61

Table 3
Run-time comparison for SD7003 aerofoil at $Re = 6 \times 10^4$, $\alpha = 8°$, and $p = 4$ with 137 916 hexahedral elements partitioned for 32 NVIDIA V100 GPUs.

Scheme	Configuration	Wall time
ACM, $\zeta = 3$	RK3(2)4[2R+], PMG, LAPTS	1:27:01
ACM-HD, $\zeta = 3$, $T = 100\nu$	RK3(2)4[2R+], PMG, LAPTS	4:06:31
EDAC, $\zeta = 100$	RK3(2)4[2R+], GAPTS	0:45:28
EDAC, $\zeta = 20$	RK3(2)4[2R+], GAPTS	0:22:46
EDAC, $\zeta = 4$	RK3(2)4[2R+], GAPTS	0:12:46

Similarly to the cylinder test case, this case was run from $\hat{t} = 45$ to $\hat{t} = 46$, and the runtime recorded, similar to the test performed by Loppi et al. [19]; however, here NVIDIA V100 GPUs were used. The results are presented in Table 3 and there is a clear benefit to EDAC over ACM in this case, with ACM-HD being significantly slower than ACM. The reason for this is, although a larger time step can be taken, the anti-aliasing used greatly increases the cost. This is due to the large number of global reads and writes required for the flux calculation. In this case at $p = 4$, $q = 11$ anti-aliasing is used, given the flux for ACM-HD on a hexahedral element requires $d(1 + d + d^2)(q + 1)^d$ values per element, flux anti-aliasing with a high degree will require substantially more bandwidth than ACM. (See Fig. 13.)

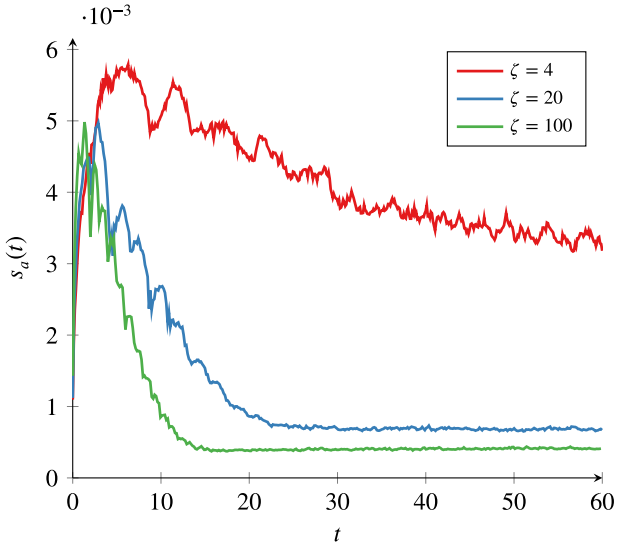

Fig. 13. Volume-averaged absolute divergence as a function of time for the SD7003 at $\alpha = 8°$, $Re = 6 \times 10^4$ and $p = 4$.

5. Conclusions

In this work we explored the properties of EDAC, the widely used ACM technique, and the hyperbolic-diffusion approach ACM-HD. The EDAC approach offers a strong mechanism to keep divergence low and can be run explicitly, without requiring the solution to a large

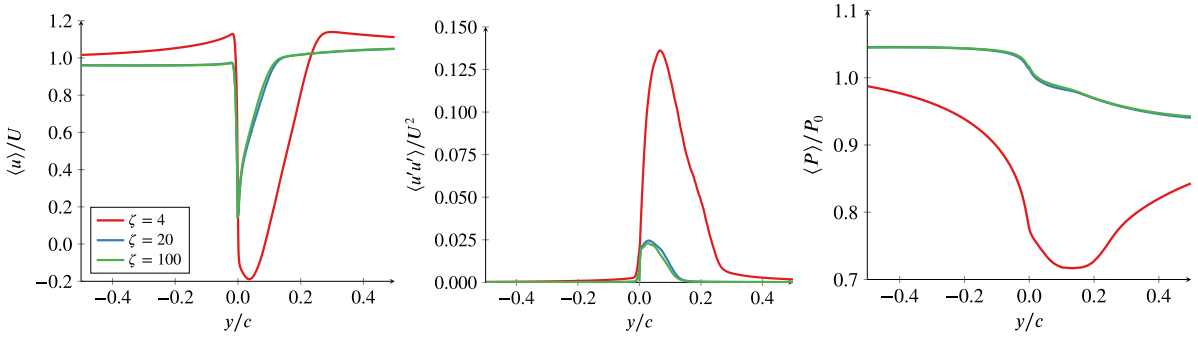

(a) $\langle u \rangle / U$. (b) $\langle u'u' \rangle / U^2$. (c) $\langle P \rangle / P_0$.

Fig. 14. Span and time averaged qualities at trailing edge of SD7003 at $Re = 6 \times 10^4$, $\alpha = 8°$, and $p = 4$. The trailing edge is centred at $y/c = 0$.

non-linear system. Novel insight into the Riemann problem for the conservative EDAC system and ACM-HD system was provided and displayed the effect the various parameters of the schemes would have on stiffness. This analysis identified some unique challenges when formulating either maximum absolute eigenvalues estimations or Riemann invariant boundary conditions in EDAC and ACM-HD.

A detailed comparison was then performed of these three methods on various turbulent flows. Using the Taylor–Green vortex case, it was shown that as the EDAC compressibility parameter (ζ) tended to infinity, the divergence scaled linearly with $\sqrt{\zeta}$, a result of the system converging to the incompressible Navier–Stokes equations. Furthermore, it was found that HLLC common interface calculations could significantly reduce divergence and increase the maximum stable time step compared to Rusanov. In contrast, for ACM and ACM-HD as ζ tended to infinity this linear relation was not observed, instead improvements in divergence diminished, a result of the non-linear solve occurring at each time-step. For higher Reynolds number flows, it was shown that EDAC with low values of ζ could lead to erroneous turbulent transition caused by the larger pressure gradients which were observed to increase turbulent production or suppress reattachment. These pressure gradients are the mechanism used to control velocity divergence and are inherent to the EDAC method. As an example of this, the circular cylinder at $Re = 3900$ with EDAC ($\zeta = 20$) was simulated and transition of the free-shear layer occurred significantly earlier due to over production of turbulent kinetic energy. Similar errors where observed for the SD-7003 aerofoil at $Re = 60\,000$, where low values of ζ with EDAC caused larger spatial variations of pressure which prevented boundary layer reattachment. ACM and ACM-HD simulations on the other hand did not face this problem, with ACM-HD having a comparable or faster run time than EDAC on the cylinder case due to the high stiffness induced by high ζ values. However, ACM and ACM-HD had significantly higher setup times due to the non-linear solver and tuning of the p-multigrid convergence acceleration method.

It is concluded that EDAC can be an effective alternative to ACM for unsteady problems, allowing for results quicker and with lower setup times. However, care must be taken in cases with transition and separation as these phenomena were found to be sensitive to ζ in the EDAC approach. Furthermore, the improved stability and convergence properties of ACM-HD can make more favourable compared to ACM.

CRediT authorship contribution statement

W. Trojak: Conceptualization, Methodology, Software, Formal analysis, Investigation, Writing – original draft, Writing – review & editing, Visualization, Funding acquisition. **N.R. Vadlamani:** Conceptualization, Methodology, Writing – original draft, Writing – review & editing. **J. Tyacke:** Conceptualization, Methodology, Writing – original draft, Writing – review & editing, Visualization. **F.D. Witherden:** Writing – original draft, Writing – review & editing, Visualization, Supervision, Project administration, Funding acquisition, Resources. **A. Jameson:** Writing – original draft, Writing – review & editing, Visualization, Supervision, Project administration, Funding acquisition, Resources.

Declaration of competing interest

The authors declare the following financial interests/personal relationships which may be considered as potential competing interests: Freddie Witherden reports equipment, drugs, or supplies was provided by US Air Force Office of Scientific Research.

Data availability

Data will be made available on request.

Acknowledgements

This material is based upon work supported by, or in part by, the U. S. Air Force Office of Scientific Research DURIP program under FA9550-21-1-0190 for Enabling next-generation heterogeneous computing for massively parallel high-order compressible CFD, under the direction of Fariba Fahroo. The authors would like to gratefully acknowledge Tarik Dzanic for providing DNS data of the cylinder and proofreading, as well as Geng Tian and Zuoli Xiao for making their data available, although we did not use this in the final manuscript.

Appendix A. ACM-HD Riemann problem

To understand the structure and limitations of the Riemann problem for the ACM-HD system we focus on the 2D system. Calculating the inviscid flux Jacobian in the x direction as:

$$\frac{\partial \mathbf{f}}{\partial \mathbf{U}} = \begin{bmatrix} 0 & \zeta & 0 & 0 & 0 & 0 & 0 \\ 1 & 2u & 0 & -\nu & 0 & 0 & 0 \\ 0 & v & u & 0 & 0 & -\nu & 0 \\ 0 & -1/T & 0 & 0 & 0 & 0 & 0 \\ 0 & 0 & 0 & 0 & 0 & 0 & 0 \\ 0 & 0 & -1/T & 0 & 0 & 0 & 0 \\ 0 & 0 & 0 & 0 & 0 & 0 & 0 \end{bmatrix}. \tag{29}$$

This has the eigenvalues:

$$\lambda_1 = \lambda_2 = \lambda_3 = 0, \quad \lambda_4 = \frac{1}{2}u + c, \quad \lambda_5 = \frac{1}{2}u - c, \\ \lambda_6 = u + b, \quad \text{and} \quad \lambda_7 = u - b, \tag{30}$$

for $c^2 = u^2/4 + \nu/T$ and $b^2 = u^2 + \zeta + \nu/T$. The associated eigenvectors are

$$\mathbf{R}^{(1)} = \begin{bmatrix} 0 \\ 0 \\ 0 \\ 0 \\ 0 \\ 0 \\ 1 \end{bmatrix}, \quad \mathbf{R}^{(2)} = \begin{bmatrix} 0 \\ 0 \\ 0 \\ 0 \\ 1 \\ 0 \\ 0 \end{bmatrix}, \quad \mathbf{R}^{(3)} = \begin{bmatrix} \nu \\ 0 \\ 0 \\ 1 \\ 0 \\ 0 \\ 0 \end{bmatrix},$$

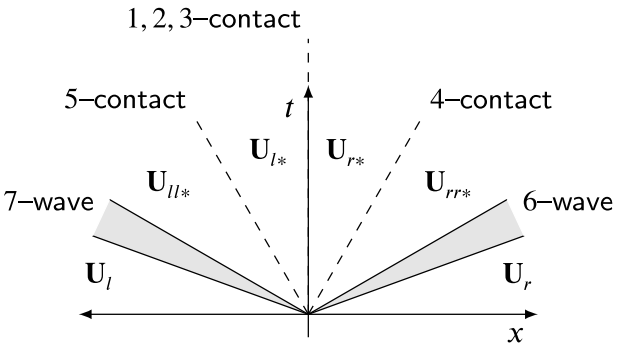

Fig. 15. Riemann fan for 2D ACM-HD.

$$\mathbf{R}^{(4)} = \frac{1}{2}\begin{bmatrix} 0 \\ 0 \\ -T(u+2c) \\ 0 \\ 0 \\ 2 \\ 0 \end{bmatrix}, \quad \mathbf{R}^{(5)} = \frac{1}{2}\begin{bmatrix} 0 \\ 0 \\ -T(u-2c) \\ 0 \\ 0 \\ 2 \\ 0 \end{bmatrix}.$$

$$\mathbf{R}^{(6)} = \begin{bmatrix} \zeta \\ u+b \\ \tilde{v}(u+b)^2/(a^2+bu) \\ -1/T \\ 0 \\ -v(u+b)/T(a^2+bu) \\ 0 \end{bmatrix}, \quad \mathbf{R}^{(7)} = \begin{bmatrix} \zeta \\ u-b \\ v(u-b)^2/(a^2-bu) \\ -1/T \\ 0 \\ -v(u-b)/T(a^2-bu) \\ 0 \end{bmatrix},$$

where $a = \sqrt{u^2+\zeta}$. This shows that the linear degeneracy indicated by the repeated eigenvalues $\lambda_1 = \lambda_2 = \lambda_3$, results in a stationary contact discontinuity. The discontinuous properties are q_y, r_y, as well as P and q_x. These final two are part of the same wave and so are related through a Riemann invariant. A stationary contact discontinuity makes formulating an exact Riemann solver more complex, although possible. If the purpose of the exact Riemann solver is to form an upper bound on the maximum absolute eigenvalue [52], then this is not an issue; however, it is not possible to produce a common interface value. A similar issue would be confronted by the HLLC method and a linearisation of the central contact would be necessary. The structure of the 2D ACM-HD Riemann problem is shown in Fig. 15, given that:

$$\lambda_7 \leqslant \lambda_5 \leqslant 0 \leqslant \lambda_4 \leqslant \lambda_6. \tag{31}$$

Appendix B. EDAC Riemann problem

To understand the structure of the wave fan for EDAC and devise Riemann solvers, we will first state the Riemann problem:

$$\partial_t \mathbf{Q} + \partial_x(\mathbf{F}^{\mathbf{inv}} \cdot \mathbf{n}) = 0, \quad \text{for} \quad \mathbf{n} \in \mathcal{B}(1,0), \quad \text{and} \quad \mathbf{Q}_0 = \begin{cases} \mathbf{Q}_L, & \text{if } x < 0, \\ \mathbf{Q}_R, & \text{otherwise,} \end{cases} \tag{32}$$

Using a transformation to the reference problem $\hat{\mathbf{n}} = [1,0,0]^T$, we can form general solutions to the Riemann problem by only studying the first column vector for the inviscid flux, $\mathbf{f} = \mathbf{F}^{\text{inv}} \cdot \hat{\mathbf{n}}$. The Jacobian of the conservative formulation of EDAC can be straightforwardly found as

$$\frac{\partial \mathbf{f}}{\partial \mathbf{Q}} = \begin{bmatrix} u & P+\zeta & 0 & 0 \\ 1 & 2u & 0 & 0 \\ 0 & v & u & 0 \\ 0 & w & 0 & u \end{bmatrix}, \tag{33}$$

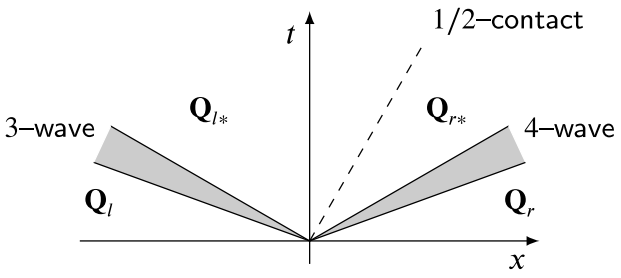

Fig. 16. Riemann fan for conservative EDAC formulation.

which has the eigenvalues

$$\lambda_1 = \lambda_2 = u, \quad \lambda_3 = \frac{3}{2}u - d, \quad \text{and} \quad \lambda_4 = \frac{3}{2}u + d, \tag{34}$$

for $d^2 = u^2/4 + P + \zeta$. The associated right eigenvectors are:

$$\mathbf{K}_1 = \begin{bmatrix} 0 \\ 0 \\ 0 \\ 1 \end{bmatrix}, \quad \mathbf{K}_2 = \begin{bmatrix} 0 \\ 0 \\ 1 \\ 0 \end{bmatrix}, \quad \mathbf{K}_3 = \begin{bmatrix} P+\zeta \\ u/2-d \\ v \\ w \end{bmatrix}, \quad \mathbf{K}_4 = \begin{bmatrix} P+\zeta \\ u/2+d \\ v \\ w \end{bmatrix}. \tag{35}$$

This combination of eigenvalues and eigenvectors tells use that the Riemann problem for this case does have a linear degeneracy, in that it can support a contact discontinuity in v and w, the structure can be seen more clearly in Fig. 16. With this established, the strategy to form an exact Riemann solver will follow a similar procedure to Elsworth and Toro [31]. We will include the main steps of the procedure as there are some interesting differences compared to the standard ACM formulation.

B.1. Exact solution

The first stage of the exact Riemann solver is to find the non-linear equation that governs u_*, this has the general form

$$0 = P_L - P_R + f_L(u_*) + f_R(u_*) = F_*(u_*) \tag{36}$$

where $f_L(u_*) = P_* - P_L$, and $f_R(u_*) = P_R - P_*$. Solving this will give u_* and P_*. The i-waves 3 and 4 can be either rarefactions or shock waves and f will depend on the wave type. We will start by finding f for the case when the waves are rarefactions.

B.1.1. Rarefaction

Taking the Riemann invariant across the 3-wave, we find that:

$$\frac{\mathrm{d}P}{\mathrm{d}u} = -\left(d + \frac{u}{2}\right), \tag{37}$$

This has the general solution:

$$P = C^2 + Cu - \zeta, \tag{38}$$

for some constant C. There is a special case when $C = -u/2$ and hence we find that:

$$P_* - P_L = \frac{1}{4}(u_L^2 - u_*^2), \quad \text{and} \quad \frac{\mathrm{d}}{\mathrm{d}u_*}(P_* - P_L) = -\frac{1}{2}u_*. \tag{39}$$

This process can be repeated for the 4-wave, to give a similar solution

$$\frac{\mathrm{d}P}{\mathrm{d}u} = d - u/2 \quad \Longrightarrow \quad P = -\frac{u^2}{4} - \zeta, \tag{40}$$

which yields

$$P_R - P_* = \frac{1}{4}(u_*^2 - u_R^2), \quad \text{and} \quad \frac{\mathrm{d}}{\mathrm{d}u_*}(P_R - P_*) = -\frac{1}{2}u_*. \tag{41}$$

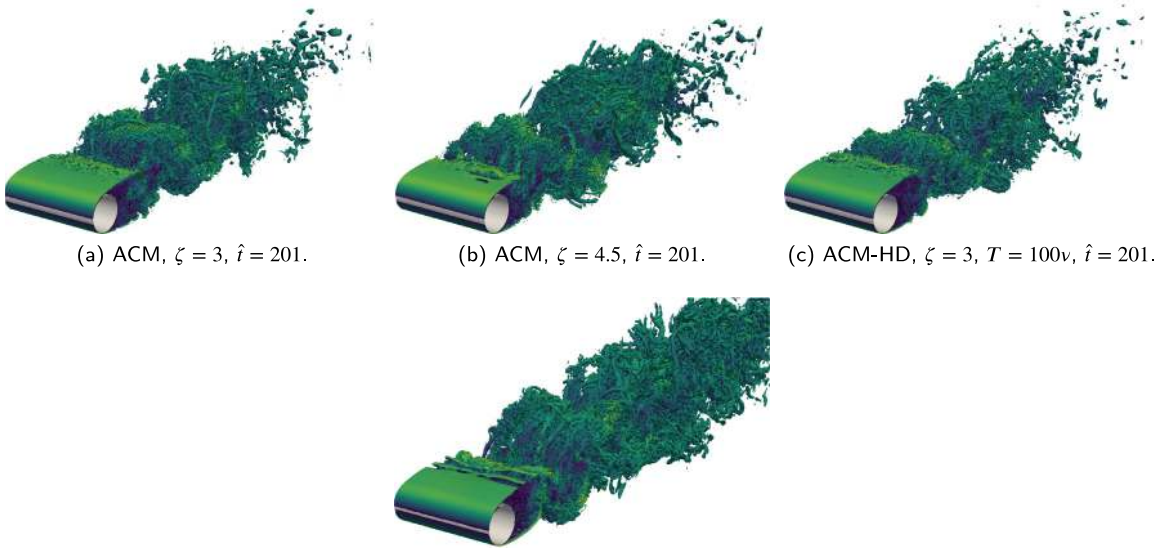

(a) ACM, $\zeta = 3$, $\hat{t} = 201$. (b) ACM, $\zeta = 4.5$, $\hat{t} = 201$. (c) ACM-HD, $\zeta = 3$, $T = 100\nu$, $\hat{t} = 201$.

(d) DNS, $\hat{t} = 350$.

Fig. 17. Iso-contours of Q-criterion, $Q = 0.1$, coloured by velocity magnitude, DNS data courtesy of Dzanic et al. [44].

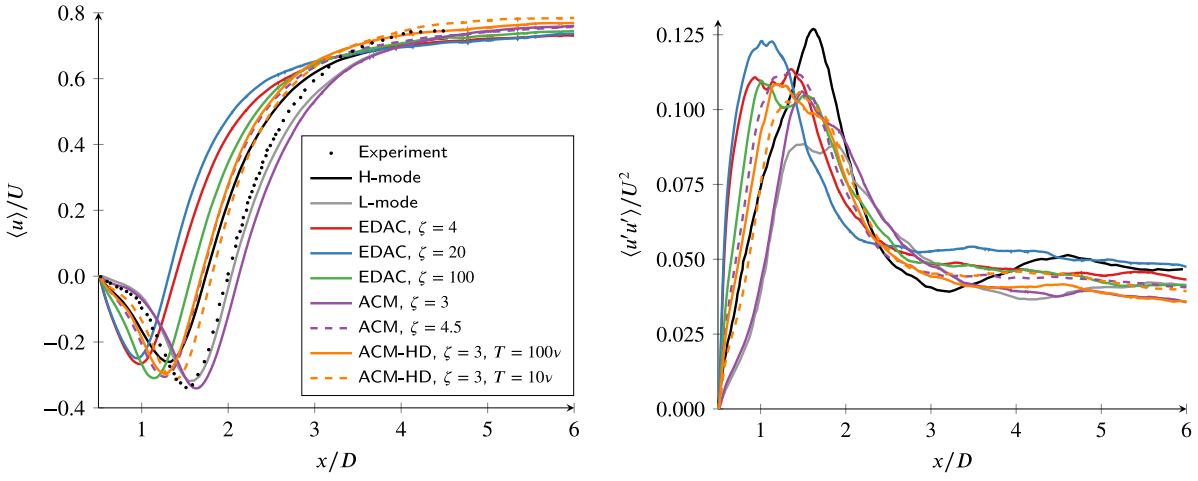

(a) $\langle u \rangle / U$ (b) $\langle u'u' \rangle / U^2$

Fig. 18. Centreline average quantities, with experimental data from Parnaudeau et al. [45] and DNS data from Lehmkuhl et al. [42].

B.1.2. Shock

For the shock case, we apply the Rankine–Hugoniot condition, therefore considering the 3-wave we have

$$S_L = \frac{u_L(P_L + \zeta) - u_*(P_* + \zeta)}{P_L - P_*} \tag{42a}$$

$$S_L = \frac{u_L^2 + P_L - u_*^2 - P_*}{u_L - u_*} \tag{42b}$$

Eliminating S_L and factoring in terms of $P_* - P_L$ we obtain the quadratic

$$(P_* - P_L)^2 + u_L(u_* - u_l)(P_* - P_L) - (P_L + \zeta)(u_* - u_L)^2 = 0. \tag{43}$$

Solving this gives solutions:

$$P_* - P_L = (u_* - u_l)\left[-\frac{u_L}{2} \pm d_L\right]$$

To select the physical solution, we use consider the entropy condition across the 3-wave, implying that

$$\frac{3}{2}u_L - d_L > S_L > \frac{3}{2}u_* - d_*.$$

This is only satisfied by one of the solutions, therefore we find that

$$P_* - P_L = -(u_* - u_l)\left(\frac{u_L}{2} + d_L\right), \quad \text{and} \frac{\mathrm{d}}{\mathrm{d}u_*}(P_* - P_L) = -\left(\frac{u_L}{2} + d_L\right). \tag{44}$$

Repeating this process for the 4-wave with the alternative entropy condition of

$$\frac{3}{2}u_R + d_R > S_R > \frac{3}{2}u_* + d_*,$$

we find that

$$P_R - P_* = (u_R - u_*)\left(-\frac{u_R}{2} + d_R\right), \quad \text{and} \quad \frac{\mathrm{d}}{\mathrm{d}u_*}(P_R - P_*) = \left(\frac{u_R}{2} - d_R\right). \tag{45}$$

The condition on whether a wave is a shock or rarefaction is based on the wavespeeds either side of the i-wave. This gives

$$\text{Left wave} = \begin{cases} \text{Rarefaction} & \text{if } \lambda_3(u_L, P_L) < \lambda_3(u_*, P_{*L}), \\ \text{Shock} & \text{otherwise,} \end{cases} \tag{46}$$

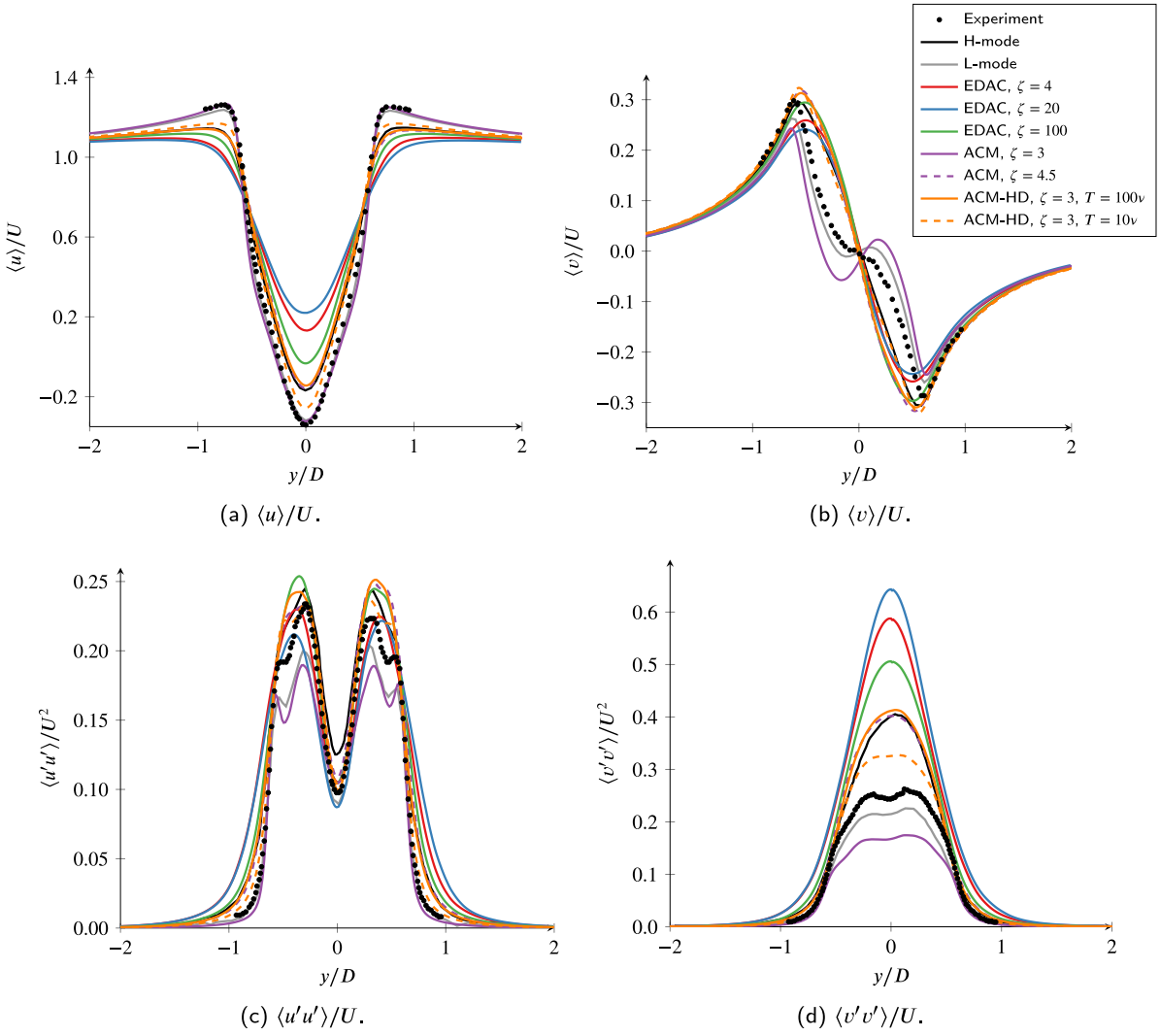

(a) $\langle u \rangle / U$. (b) $\langle v \rangle / U$.

(c) $\langle u'u' \rangle / U$. (d) $\langle v'v' \rangle / U$.

Fig. 19. $x/D = 1.54$, with experimental data from Parnaudeau et al. [45] and DNS data from Lehmkuhl et al. [42].

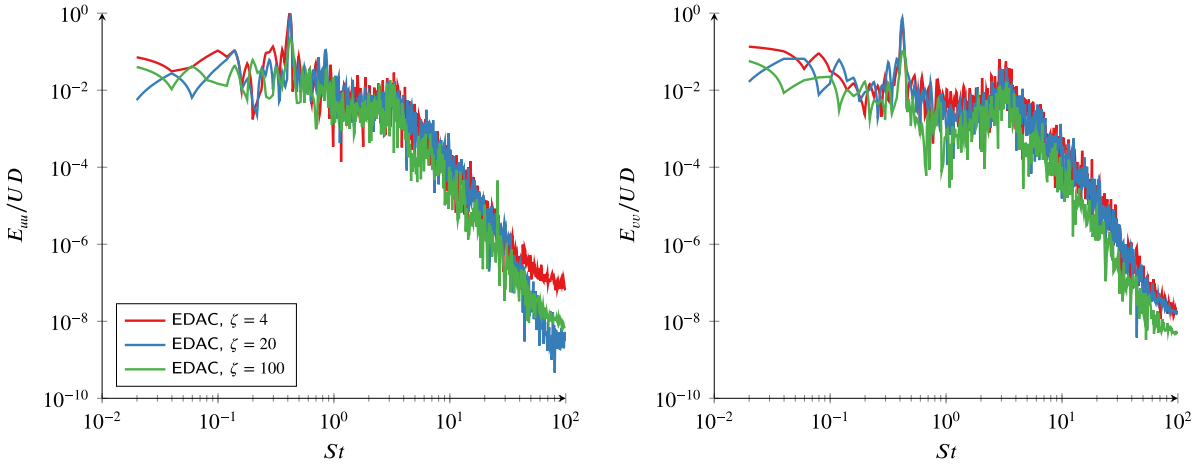

(a) Stream-wise velocity. (b) Span-wise velocity.

Fig. 20. Power spectral density at $\mathbf{x} = (0.71D, 0.66D, 1.57D)$.

and

$$\text{Right wave} = \begin{cases} \text{Rarefaction} & \text{if } \lambda_4(u_*, P_{*R}) < \lambda_4(u_R, P_{*R}), \\ \text{Shock} & \text{otherwise.} \end{cases} \tag{47}$$

To solve Eq. (36) Newton's method can be applied and in the limit of convergence $P_{*L} = P_{*R} = P_*$.

B.2. HLL and HLLC Riemann solver

A common approach taken to design a low dissipation approximate Riemann solver is to use the HLL and HLLC approaches first described by Harten et al. [53]. The HLL approach assumes that all variables are constant in the region that is bound by the extreme i-waves. The speeds of these waves is approximated using a Davis approximation as

$$\begin{aligned} S_L &= \min\left(\frac{3}{2}u_L - d_L, \frac{3}{2}u_R - d_R\right), \quad \text{and} \\ S_R &= \max\left(\frac{3}{2}u_L + d_L, \frac{3}{2}u_R + d_r\right), \end{aligned} \tag{48}$$

and the star flux takes the standard form:

$$\mathbf{f}_* = \frac{S_R\mathbf{f}_L - S_L\mathbf{f}_R + S_LS_R(\mathbf{u}_R - \mathbf{U}_L)}{S_R - S_L}. \tag{49}$$

This gives the HLL reconstruction as

$$\mathbf{f}_{\text{HLL}} = \begin{cases} \mathbf{f}_L & \text{if } 0 \leqslant S_L \\ \mathbf{f}_* & \text{if } S_L < 0 < S_R \\ \mathbf{f}_R & \text{if } S_R \leqslant 0. \end{cases} \tag{50}$$

The HLLC approach instead models the contact discontinuity, however in the star region u and P are constant, hence, we will use the HLL method to approximate u_* and P_*. Therefore taking:

$$P_{*L} = P_{*R} = P_*, \quad \text{and} \quad u_{*L} = u_{*R} = S_*, \tag{51}$$

then From the Rankine–Hugoniot condition we have that

$$\mathbf{f}_{*L} = S_L(\mathbf{U}_{*L} - \mathbf{U}_L) + \mathbf{f}_L, \tag{52a}$$

$$\mathbf{f}_{*R} = S_R(\mathbf{U}_{*R} - \mathbf{U}_R) + \mathbf{f}_R. \tag{52b}$$

These can be used to find the closed relations for S_* and P_* as

$$\begin{aligned} S_* &= \frac{S_LS_R(P_L - P_R) - S_Ru_L(P_L + \zeta) + S_Lu_R(P_R + \zeta)}{(S_L - u_L)(P_L + \zeta) - (S_R - u_R)(P_R + \zeta)}, \quad \text{and} \\ P_* &= \left(\frac{S_L - u_L}{S_L - S_*}\right)\left(P_L + \left[\frac{S_* - u_L}{S_L - u_L}\right]\zeta\right). \end{aligned} \tag{53}$$

The tangential velocity components can then be found as

$$v_{*x} = \left(\frac{S_x - u_x}{S_x - S_*}\right)v_x, \quad \text{and} \quad w_{*x} = \left(\frac{S_x - u_x}{S_x - S_*}\right)w_x, \tag{54}$$

where x is L or R. The complete star states can then be written as

$$\mathbf{U}_{*x} = \Gamma_x\begin{bmatrix} P_L + \zeta(S_* - u_x)/(S_x - u_x) \\ S_*/\Gamma_x \\ v_x \\ w_x \end{bmatrix}, \quad \text{for} \quad \Gamma_x = \frac{S_x - u_x}{S_x - S_*}, \tag{55}$$

and the final scheme is

$$\mathbf{f}_{\text{HLLC}} = \begin{cases} \mathbf{f}_L & \text{if } 0 \leqslant S_L \\ \mathbf{f}_{*L} & \text{if } S_L < 0 \leqslant S_* \\ \mathbf{f}_{*R} & \text{if } S_* < 0 < S_R \\ \mathbf{f}_R & \text{if } S_R \leqslant 0 \end{cases} \tag{56}$$

The most straightforward means to apply these approximate Riemann solvers is by transforming the solution from the normal $\hat{\mathbf{n}}$ to a reference normal, $[1, 0, 0]^T$, calculating $\mathbf{f}$ and then transforming back again. In two-dimensions this is trivial, however, in three-dimensions this transformation can suffer from numerical errors. A fix for this issue is the approach of Möller and Hughes [54], there Householder transformations are used when the normal vector is closely aligned to either of the tangential cardinal directions.

B.3. Riemann invariant boundary condition

Now that the Riemann structure is understood, a Riemann invariant boundary condition can be defined. The invariants are

$$R_- = P_i + \frac{1}{4}(u_i^\perp)^2 + \zeta, \quad \text{and} \quad R_+ = P_e + \frac{1}{4}(u_e^\perp)^2 + \zeta, \tag{57}$$

where i is the interior state and e is the exterior state. The invariants clearly show that the system cannot support a solution with two rarefactions. Instead to apply a boundary condition a full solve for the Riemann problem is performed to get $u_b^\perp$ and P_b based on the interior left state $u_i^\perp$, P_i, and the exterior right state $u_e^\perp$, P_e. The velocity at the boundary is then:

$$\mathbf{V}_b = \begin{cases} \mathbf{V}_i + \hat{\mathbf{n}}(u_b^\perp - \hat{\mathbf{n}} \cdot \mathbf{V}_i) & \text{if } \hat{\mathbf{n}} \cdot \mathbf{V}_i, \\ \mathbf{V}_e + \hat{\mathbf{n}}(u_b^\perp - \hat{\mathbf{n}} \cdot \mathbf{V}_e) & \text{otherwise.} \end{cases} \tag{58}$$

Appendix C. Additional cylinder plots

See Figs. 17–20.

Appendix D. Supplementary data

Supplementary material related to this article can be found online at https://doi.org/10.1016/j.compfluid.2022.105634.

References

[1] Vincent P, Witherden F, Vermeire B, Park JS, Iyer A. Towards Green aviation with Python at petascale. In: SC16: International conference for high performance computing, networking, storage and analysis. 2016.

[2] Kim S, Alonso J, Jameson A. Design optimization of high-lift configurations using a viscous continuous adjoint method. In: 40th AIAA aerospace sciences meeting & exhibit. American Institute of Aeronautics and Astronautics (AIAA); 2002, http://dx.doi.org/10.2514/6.2002-844.

[3] Williams T, Hall C, Wilson M. Low pressure ratio transonic fan stall with radial distortion. J Global Power Propuls Soc 2020;4:226–37. http://dx.doi.org/10.33737/jgpps/130478.

[4] Durbin PA. Some recent developments in turbulence closure modeling. Annu Rev Fluid Mech 2018;50:77–103. http://dx.doi.org/10.1146/annurev-fluid-122316-045020.

[5] Huynh HT. A flux reconstruction approach to high-order schemes including discontinuous Galerkin methods. In: 18th AIAA computational fluid dynamics conference. American Institute of Aeronautics and Astronautics; 2007, http://dx.doi.org/10.2514/6.2007-4079.

[6] Witherden FD, Farrington AM, Vincent PE. PyFR: An open source framework for solving advection–diffusion type problems on streaming architectures using the flux reconstruction approach. Comput Phys Comm 2014;185:3028–40. http://dx.doi.org/10.1016/j.cpc.2014.07.011.

[7] Roe PL. Approximate Riemann solvers, parameter vectors, and difference schemes. J Comput Phys 1981;43:357–72. http://dx.doi.org/10.1016/0021-9991(81)90128-5.

[8] Turkel E. Preconditioned methods for solving the incompressible and low speed compressible equations. J Comput Phys 1987;72:277–98. http://dx.doi.org/10.1016/0021-9991(87)90084-2.

[9] Fortunato D, Townsend A. Fast Poisson solvers for spectral methods. IMA J Numer Anal 2019;40:1994–2018. http://dx.doi.org/10.1093/imanum/drz034.

[10] Elman H, Silvester D, Wathen A. The Stokes equations. In: Finite elements and fast iterative solvers: With applications in incompressible fluid dynamics. Oxford University Press; 2014, p. 119–88. http://dx.doi.org/10.1093/acprof:oso/9780199678792.003.0004.

[11] Chorin AJ. A numerical method for solving incompressible viscous flow problems. J Comput Phys 1967;2:12–26. http://dx.doi.org/10.1016/0021-9991(67)90037-x.

[12] Rogers SE, Kwak D, Kiris C. Steady and unsteady solutions of the incompressible Navier-Stokes equations. 1991;29:603–10. http://dx.doi.org/10.2514/3.10627.

[13] Jameson A. Time dependent calculations using multigrid, with applications to unsteady flows past airfoils and wings. In: 10th computational fluid dynamics conference. American Institute of Aeronautics and Astronautics; 1991, http://dx.doi.org/10.2514/6.1991-1596.

[14] Shapiro E, Drikakis D. Artificial compressibility, characteristics-based schemes for variable density, incompressible, multi-species flows. Part I. Derivation of different formulations and constant density limit. J Comput Phys 2005;210:584–607. http://dx.doi.org/10.1016/j.jcp.2005.05.001.

[15] Shapiro E, Drikakis D. Artificial compressibility, characteristics-based schemes for variable-density, incompressible, multispecies flows: Part II. Multigrid implementation and numerical tests. J Comput Phys 2005;210:608–31. http://dx.doi.org/10.1016/j.jcp.2005.05.002.

[16] Nishikawa H. A first-order system approach for diffusion equation. I: Second-order residual-distribution schemes. J Comput Phys 2007;227:315–52. http://dx.doi.org/10.1016/j.jcp.2007.07.029.

[17] Ahn HT. Hyperbolic cell-centered finite volume method for steady incompressible Navier-Stokes equations on unstructured grids. Comput & Fluids 2020;200:104434. http://dx.doi.org/10.1016/j.compfluid.2020.104434.

[18] Trojak W, Watson R, Witherden F. Hyperbolic diffusion in flux reconstruction: Optimisation through kernel fusion within tensor-product elements. 2021, https://arxiv.org/abs/2107.14027.

[19] Loppi NA, Witherden FD, Jameson A, Vincent PE. Locally adaptive pseudo-time stepping for high-order flux reconstruction. J Comput Phys 2019;399:108913. http://dx.doi.org/10.1016/j.jcp.2019.108913.

[20] Loppi N. High-order incompressible computational fluid dynamics on modern hardware architectures. Cassyni; 2021, http://dx.doi.org/10.52843/cassyni.y2hggy.

[21] Clausen JR. Entropically damped form of artificial compressibility for explicit simulation of incompressible flow. Phys Rev E 2013;87. http://dx.doi.org/10.1103/physreve.87.013309.

[22] Achu S, Vadlamani NR. Entropically damped artificial compressibility solver using higher order finite difference schemes on curvilinear and deforming meshes. In: AIAA scitech 2021 forum. 2021.

[23] Toutant A. Numerical simulations of unsteady viscous incompressible flows using general pressure equation. J Comput Phys 2018;374:822–42. http://dx.doi.org/10.1016/j.jcp.2018.07.058.

[24] Dupuy D, Toutant A, Bataille F. Analysis of artificial pressure equations in numerical simulations of a turbulent channel flow. J Comput Phys 2020;411:109407. http://dx.doi.org/10.1016/j.jcp.2020.109407.

[25] Moura RC, Mengaldo G, Peiró J, Sherwin SJ. On the eddy-resolving capability of high-order discontinuous Galerkin approaches to implicit LES / under-resolved DNS of Euler turbulence. J Comput Phys 2017;330:615–23. http://dx.doi.org/10.1016/j.jcp.2016.10.056.

[26] Williams DM, Jameson A. Energy stable flux reconstruction schemes for advection–diffusion problems on tetrahedra. J Sci Comput 2013;59:721–59. http://dx.doi.org/10.1007/s10915-013-9780-2.

[27] Witherden F. On the development and implementation of high-order flux reconstruction schemes for computational fluid dynamics [Ph.D. thesis], Imperial College London; 2015.

[28] Toro EF. Riemann solvers and numerical methods for fluid dynamics. Springer Berlin Heidelberg; 2009, http://dx.doi.org/10.1007/b79761.

[29] Kennedy CA, Carpenter MH, Lewis RM. Low-storage, explicit Runge–Kutta schemes for the compressible Navier–Stokes equations. Appl Numer Math 2000;35:177–219. http://dx.doi.org/10.1016/s0168-9274(99)00141-5.

[30] Hairer E, Nørsett SP, Wanner G. Solving ordinary differential equations I. Springer Berlin Heidelberg; 1993, http://dx.doi.org/10.1007/978-3-540-78862-1.

[31] Elsworth DT, Toro EF. Riemann Solvers for Solving the Incompressible Navier–Stokes Equations Using the Artificial Compressibility Method. Technical Report 9208, Cranfield University; 1992.

[32] Nishikawa H, Liu Y. Hyperbolic advection–diffusion schemes for high-Reynolds-number boundary-layer problems. J Comput Phys 2018;352:23–51. http://dx.doi.org/10.1016/j.jcp.2017.09.039.

[33] Dafermos CM. Hyperbolic conservation laws in continuum physics. 2nd ed.. Springer Berlin Heidelberg; 2005, p. 67–86. http://dx.doi.org/10.1007/978-3-662-49451-6.

[34] Taylor GI, Green AE. Mechanism of the production of small eddies from large ones. Proc R Soc Lond Ser A Math Phys Eng Sci 1937;158:499–521. http://dx.doi.org/10.1098/rspa.1937.0036.

[35] Brachet ME, Meiron DI, Orszag SA, Nickel BG, Morf RH, Frisch U. Small-scale structure of the Taylor–Green vortex. J Fluid Mech 1983;130:411. http://dx.doi.org/10.1017/s0022112083001159.

[36] Loppi NA, Witherden FD, Jameson A, Vincent PE. A high-order cross-platform incompressible Navier–Stokes solver via artificial compressibility with application to a turbulent jet, 2018;233:193–205, http://dx.doi.org/10.1016/j.cpc.2018.06.016.

[37] Trojak W, Witherden FD. On Fourier analysis of polynomial multigrid for arbitrary multi-stage cycles. 2020, arXiv:arXiv:2008.05463.

[38] van Rees WM, Leonard A, Pullin DI, Koumoutsakos P. A comparison of vortex and pseudo-spectral methods for the simulation of periodic vortical flows at high Reynolds numbers. J Comput Phys 2011;230:2794–805. http://dx.doi.org/10.1016/j.jcp.2010.11.031.

[39] Toro EF, Müller LO, Siviglia A. Bounds for wave speeds in the Riemann problem: Direct theoretical estimates. Comput & Fluids 2020;209:104640. http://dx.doi.org/10.1016/j.compfluid.2020.104640.

[40] Williamson CHK. Vortex dynamics in the cylinder wake. Annu Rev Fluid Mech 1996;28:477–539. http://dx.doi.org/10.1146/annurev.fl.28.010196.002401.

[41] Pereira FS, Vaz G, Eça L, Girimaji SS. Simulation of the flow around a circular cylinder at $Re = 3900$ with partially-averaged Navier-Stokes equations. Int J Heat Fluid Flow 2018;69:234–46. http://dx.doi.org/10.1016/j.ijheatfluidflow.2017.11.001.

[42] Lehmkuhl O, Rodríguez I, Borrell R, Oliva A. Low-frequency unsteadiness in the vortex formation region of a circular cylinder. Phys Fluids 2013;25:085109. http://dx.doi.org/10.1063/1.4818641.

[43] Vermeire BC, Witherden FD, Vincent PE. On the utility of GPU accelerated high-order methods for unsteady flow simulations: A comparison with industry-standard tools. J Comput Phys 2017;334:497–521. http://dx.doi.org/10.1016/j.jcp.2016.12.049.

[44] Dzanic T, Girimaji S, Witherden F. Partially-averaged Navier-Stokes simulations of turbulence within a high-order flux reconstruction framework. J. Comput. Phys. 2022;456:110992. http://dx.doi.org/10.1016/j.jcp.2022.110992.

[45] Parnaudeau P, Carlier J, Heitz D, Lamballais E. Experimental and numerical studies of the flow over a circular cylinder at Reynolds number 3900. Phys Fluids 2008;20:085101. http://dx.doi.org/10.1063/1.2957018.

[46] Tian G, Xiao Z. New insight on large-eddy simulation of flow past a circular cylinder at subcritical Reynolds number 3900. AIP Adv 2020;10:085321. http://dx.doi.org/10.1063/5.0012358.

[47] Selig MS, Donovan JF, Fraser DB. Airfoils at low speeds. 1st ed.. Virginia Beach, VA:SoarTech Publications. p. 312–20.

[48] Beck AD, Bolemann T, Flad D, Frank H, Gassner GJ, Hindenlang F, et al. High-order discontinuous Galerkin spectral element methods for transitional and turbulent flow simulations. Internat J Numer Methods Fluids 2014;76:522–48. http://dx.doi.org/10.1002/fld.3943.

[49] Galbraith M, Visbal M. Implicit large eddy simulation of low-Reynolds-number transitional flow past the SD7003 airfoil. In: 40th fluid dynamics conference and exhibit. American Institute of Aeronautics and Astronautics; 2010, http://dx.doi.org/10.2514/6.2010-4737.

[50] Garmann DJ, Visbal MR, Orkwis PD. Comparative study of implicit and subgrid-scale model large-eddy simulation techniques for low-Reynolds number airfoil applications. Internat J Numer Methods Fluids 2012;71:1546–65. http://dx.doi.org/10.1002/fld.3725.

[51] Spiegel SC, Huynh HT, DeBonis JR. De-aliasing through over-integration applied to the flux reconstruction and discontinuous Galerkin methods. In: 22nd AIAA computational fluid dynamics conference. American Institute of Aeronautics and Astronautics; 2015, http://dx.doi.org/10.2514/6.2015-2744.

[52] Guermond J-L, Popov B. Fast estimation from above of the maximum wave speed in the Riemann problem for the Euler equations, 2016;321:908–26. http://dx.doi.org/10.1016/j.jcp.2016.05.054.

[53] Harten A, Lax PD, van Leer B. On upstream differencing and Godunov-type schemes for hyperbolic conservation laws. SIAM Rev 1983;25:35–61. http://dx.doi.org/10.1137/1025002.

[54] Möller T, Hughes JF. Efficiently building a matrix to rotate one vector to another. J Graph Tools 1999;4:1–4. http://dx.doi.org/10.1080/10867651.1999.10487509.